Revision 3

Metal source and hydrothermal evolution of the Jiaoxi quartz vein-type tungsten deposit (Tibet): Insights from textural and compositional variations of wolframite and scheelite

YONG WANG[1,2], CHUANKAI HE[1], JUXING TANG[2], JAN MARTEN HUIZENGA[3,4,5], LIQIANG WANG[2], XINGHAI LANG[1]

[1]College of Earth Science, Chengdu University of Technology, Chengdu, 610059, China

[2] MNR Key Laboratory of Metallogeny and Mineral Assessment, Institute of Mineral Resources, CAGS, Beijing, 100037, China

[3]Faculty of Environmental Sciences and Natural Resource Management, Norwegian University of Life Sciences, P.O. Box 5003, NO-1432, Ås, Norway

[4]EGRU (Economic Geology Research Centre), James Cook University; Townsville, Queensland 4811, Australia

[5]Department of Geology, University of Johannesburg, PO Box 524, Auckland Park, 2006, South Africa

ABSTRACT

We evaluate the controlling factors of hydrothermal wolframite and scheelite precipitation in the quartz vein-type Jiaoxi tungsten deposit situated in the western part of the Lhasa terrane (Tibet, China) using texture, major and trace element mineral geochemistry, and sulfur stable isotope geochemistry. Pyrite and chalcopyrite that are

intergrown with Fe-enriched wolframite and siderite, have distinct in situ S isotope compositions ($\delta^{34}S_{V\text{-}CDT}$) of −31.38 to +1.77‰, and +2.07 to +2.30‰, respectively. Major and trace element contents and in situ S isotope compositions of pyrite and chalcopyrite indicate that the hydrothermal evolution involved fluid-fluid mixing and greisenization. We report evidence for an early magmatic fluid which is characterized by the enrichment of W, Mn, Zr, Ti, Sc, and Sn and depletion of Fe. This magmatic fluid was diluted by meteoric water and interacted with biotite monzogranite porphyry to leach Fe, Mg, and Zn into the system to form wolframites with variable Fe/(Fe+Mn) ratios ranging between 0.06-0.84. The late Fe-enriched magmatic fluid released from the muscovite granite mixed with meteoric water that leached minor Fe and S from shale to form late shale-hosted wolframite with a Fe/(Fe+Mn) mass ratio of > 0.75 and coeval siderite and sulfides. This study highlights that multiple Fe sources were present in the system, including muscovite granite-released Fe through fluid exsolution, biotite monzogranite porphyry-released Fe during greisenization, and minor Fe released from the shale as a result of meteoric water leaching.

Key words: Wolframite, scheelite, trace element geochemistry, in situ S isotope, multiple Fe sources, Jiaoxi quartz vein-type W deposit

INTRODUCTION

Quartz vein-type tungsten (W) deposits represent a major class of hydrothermal deposits and typically occur as wolframite-bearing quartz veins hosted either in pelitic

rocks or in granites (Wang et al. 2010; Mao et al. 2013). Generally, tungsten is considered to be sourced from Fe-depleted highly evolved felsic magmatic rocks that are spatially associated with the deposit (Romer and Kroner 2016; Hulsbosch et al. 2016). However, formation of wolframite [(Fe, Mn)WO_4] does not only require W but also significant Fe and Mn in the ore-forming fluid. Therefore, tracing the source of Fe and Mn in quartz vein-type wolframite deposits has long been a subject of interest (Audétat et al. 2000; Lecumberri-Sanchez et al. 2017; Legros et al. 2019; Pan et al. 2019). However, there is no consensus on the origin of the metals because the pristine signature of the primary fluid is overprinted by multiple post-mineralization fluid events in numerous deposits (Polya et al. 2000; Harlaux et al. 2018). Recently, in situ high spatial microanalysis of W-bearing mineral phases, using multi-collector laser-ablation inductively coupled-plasma mass spectrometry (MC-LA-ICP-MS), has been used to identify multiple fluid infiltration events and the metal source (Wang et al. 2017; Hong et al. 2017; Jiang et al. 2021; Carocci et al. 2021).

Wolframite and scheelite, which can accommodate a wide range of trace elements including Ti, Sc, Zr, Hf, Nb, Ta, and REE, have been studied to constrain the hydrothermal evolution and metal sources (e.g., Kempe and Wolf 2006; Song et al. 2014; Zhu et al. 2014; Xiong et al. 2017; Sun and Chen 2017; Han et al. 2020). For example, the negative Eu anomaly of wolframite has been interpreted to be inherited from a highly evolved granite, thus indicating a magmatic source (Harlaux et al. 2018). Scheelite that precipitated from a highly evolved granite-exsolved fluid is generally Sr-depleted such that the variability of the Sr content in scheelite indicates

67 formation in a metamorphic environment, in which the metasedimentary or volcanic
68 source rocks can release Sr into the hydrothermal system (Poulin et al., 2018).
69 Although trace element contents in wolframite and scheelite have widely been
70 reported, comprehensive studies of both minerals in order to constrain the
71 hydrothermal evolution and the metal sources are rare (e.g., Zhang et al., 2018).

72 The Jiaoxi quartz vein-type W deposit is located in the western part of the Lhasa
73 terrane (Tibet, China) (Fig. 1a) (Wang et al. 2019). Scheelite, and in particular
74 wolframite, are the most important ore minerals in the Jiaoxi deposit. Different
75 wolframite and scheelite generations in this deposit display distinct chemical zonation.
76 As such, they provide an ideal opportunity to trace the metal sources and constrain the
77 hydrothermal mineralization process.

78 Here we present (1) textural results (optical microscopy, backscattered electron
79 and cathodoluminescence imaging), (2) major and trace element geochemistry of
80 wolframite and scheelite from the different mineralization stages, (3) sulphur stable
81 isotope geochemistry of pyrite and chalcopyrite, and (4) whole-rock major and trace
82 element geochemistry of shale that hosts the W mineralized quartz veins. This study
83 highlights the multiple Fe sources that contributed to the hydrothermal system.

84

85 ## GEOLOGICAL BACKGROUND

86 ### Regional geological setting

87 The Lhasa terrane in southern Tibet provides evidence for the Mesozoic
88 (accretionary orogeny) to the Cenozoic (collisional orogeny) tectonic evolution of the

Himalayan-Tibetan orogen (Yin and Harrison 2000; Ding and Lai 2003). It contains multiple post-collisional copper, gold, lead-zinc, molybdenum, and iron ore deposits (Fig. 1a; Tang et al. 2014; Hou and Cook 2009; Hou et al. 2015; Yang et al. 2016). Zhu et al. (2011) subdivided the Lhasa terrane into a northern, central, and southern subterrane based on different basement and sedimentary cover rocks (Fig. 1a). The northern Lhasa subterrane comprises juvenile crust which, is related to crustal growth associated with the southward subduction of Bangong-Nujiang ocean plate (Zhu et al. 2011, 2016). The rocks exposed in this subterrane include Middle Triassic-Cretaceous sedimentary rocks and Cretaceous volcanic rocks (Pan et al. 2012; Wang et al. 2014).

The Central Lhasa subterrane is situated between the Shiqianhe River-Nam Tso Mélange zone to the north and the Luobadui-Milashan fault to the south. It contains Proterozoic-Archean basement and widespread Paleozoic to Early Cretaceous sedimentary and volcanic cover rocks (Zhu et al. 2011; Yang et al. 2016). The southern Lhasa subterrane contains juvenile crust including the Cretaceous-Tertiary Gangdese batholith and minor Jurassic-Cretaceous volcanic rocks (Zhu et al. 2008; Yang et al. 2016).

The Jiaoxi deposit is situated in the central Lhasa subterrane in the Shiquanhe River-Nam Tso Mélange zone, ~30 km northeast of Gar County (Fig. 1a). Cretaceous strata, including the Langshan and Shiquanhe Ophiolite Mélange Groups, occur in the Shiquanhe area (Fig. 1b). The locally strongly deformed Langshan Group comprises limestone and marble and unconformably overlies the Shiquanhe Ophiolite Mélange Group. The Shiquanhe Ophiolite Mélange Group comprises shale, sandstone, slate,

111 chert, and (ultra) basic rocks, including basalt, gabbro, serpentinized dunite, and tuff.
112 These rocks underwent local greenschist-facies metamorphism during the Late
113 Cretaceous and Early Cenozoic continental collisions of the Qiangtang and Lhasa
114 terranes, and the India and Asia continents, respectively (Fig. 1b; Yin and Harrison
115 2000; Kapp et al. 2003, 2005, 2007). Magmatic rocks in the Shiquanhe area are
116 widespread and include Early Cretaceous porphyritic andesite, and Miocene biotite
117 monzogranite, biotite monzogranite porphyry, and pegmatite veins (Fig. 1b; Wang et
118 al. 2020). Northwest-SE and NE-SW trending fault sets have been identified (Fig. 1b).
119

120 **Geology of the Jiaoxi tungsten deposit**

121 The Jiaoxi quartz vein W deposit was discovered and explored by the
122 Geothermal Geology Team of Bureau of Exploration of Tibet in 2015. The deposit
123 contains 39,100 tons of WO_3 with a grade of 0.1-3.2% (Wang et al. 2018, 2019, 2020).
124 The host rocks of the Jiaoxi deposit belong to the Shiquanhe Group, which comprises
125 strongly deformed shale, sandstone, and ophiolite. Diabase dykes coeval with the
126 ophiolite, occur in the northeast of the ore district (Fig. 2). Various granites occur in
127 the deposit, including the 25-50 m thick biotite monzogranite porphyry (BMP) sill
128 (Online Materials Fig. OM1a), granite porphyry (GP), and muscovite granite (MG).
129 The BMP comprises 40-45% fine-grained phenocrysts of K-feldspar, plagioclase,
130 quartz, and biotite in a very fine-grained matrix made with the same mineral
131 composition. The GP comprises fine-grained phenocrysts (25-30%) of quartz,
132 plagioclase, and minor biotite in a very-fine grained matrix with the same mineral

133 composition. The equigranular MG comprises quartz, K-feldspar, plagioclase, and
134 muscovite.

135 Outcrops of the highly fractured BMP host numerous ore-bearing quartz veins
136 with greisenization halos indicating hydrothermal alteration. The BMP also hosts
137 numerous wolframite-bearing quartz veins and associated greisenization zones at
138 depth (drill cores ZK0001 and ZK2001). The GP is exposed in the southwest of the
139 ore district and appears as a single outcrop (< 0.1 km^2). Greisenization is widely
140 developed in the GP, but ore-bearing quartz veins are absent.

141 The unexposed MG is found at depth (drill core ZK2001) and hosts numerous
142 wolframite-bearing quartz veins. A clear intrusive contact between the BMP and the
143 MG is observed showing that the MG is younger than the BMP. The BMP, GP, and
144 MG yield zircon U-Pb ages of 14.1±0.3, 13.82±0.22, and 13.72±0.30 Ma, respectively
145 (Wang et al 2020). Two muscovite grains that occur in quartz veins and are intergrown
146 with wolframite, yield ^{40}Ar-^{39}Ar ages of 13.4-13.3 Ma (Wang et al. 2018).
147 Geochemical analysis results show that the MG was highly evolved with high SiO_2
148 contents (74.4-76.3 wt.%) and low Nb/Ta (2.4-2.8), and Zr/Hf (13.5-13.9) mass ratios
149 (Wang et al., 2020).

150 Hydrothermal alteration in the Jiaoxi deposit is characterized by greisenization of
151 the BMP and MG. The ore formation is characterized by extensional quartz veins
152 within the upper shales, the BMP, and the MG at depth (Online Materials Fig. OM1b).
153 More than 70 northeast trending quartz veins with a varying thickness of 5 cm to 8 m
154 have been identified at surface (Fig. 2). The gentle and steeply dipping quartz veins

155 extend for more than 400 m vertically, as revealed by drill cores ZK0001 and ZK2001
156 (Online Materials Fig. OM1). Wolframite (dominantly present) and scheelite are the
157 W-bearing ore minerals. The gangue minerals include pyrite, chalcopyrite, galena,
158 sphalerite, quartz, fluorite, phengite, topaz, and beryl. Based on vein crosscutting
159 relationships and mineral paragenesis, the Jiaoxi deposit underwent three
160 mineralization stages: the quartz-tungstate stage, the quartz-sulfide, and the
161 fluorite-carbonate stage (Wang et al. 2021a).

162 The quartz-tungstate stage is associated with the main mineralization event and
163 is characterized by quartz, wolframite, beryl, topaz, and minor fluorite. Euhedral
164 quartz is intergrown with sericite and eu- to subhedral wolframite (Figs. 3a and 3b).
165 Radial sericite is commonly intergrown with euhedral topaz, and beryl. The
166 quartz-wolframite-sericite veins are crosscut by later quartz-sulfide vein (Fig. 3c).

167 The sulfide stage is characterized by pyrite, chalcopyrite, galena, pyrrhotite, and
168 sphalerite. Field observations show that early quartz-sulfide veins are crosscut by the
169 fluorite-phengite veins (Fig. 3d).

170 The fluorite stage is characterized by fluorite, phengite, quartz, and minor calcite
171 and scheelite. Fluorite-stage phengite is typically larger in size (up to 1.5 cm) than the
172 sericite in the quartz-tungstate stage (< 0.5 cm).

173

174 ## MATERIALS AND ANALYTICAL METHODS

175 Three outcrop samples and 32 drill core samples (including 18 and 14 samples
176 from drill core ZK0001 and ZK2001, respectively) of mineralized veins and greisen

were collected for this study (Fig. 2; Online Materials Fig. OM 1). Sample preparations were done at the China University of Geosciences (Beijing). Sixty-eight thick sections (30-40 μm thick) of wolframite and scheelite from the different mineralization stages were prepared for analysis.

Electron probe microanalysis and backscattered electron imaging

Electron probe microanalysis (EPMA) of Ca, Mg, Ti, Mn, Fe, Ni, W, Mo, Nb, and Ta was performed on wolframite and scheelite using a JXA-8100 electron microprobe equipped with a wavelength-dispersive spectrometers at the Analytical Laboratory of the Beijing Research Institute of Uranium Geology. Natural and synthetic oxides including bustamite, rutile, hematite, molybdenite, rhodonite, olivine, pentlandite, scheelite, $LiTaO_3$, and $LiNbO_3$ were used for Ca, Ti, Fe, Mo, Mn, Mg, Ni, W, Ta, and Nb calibration, respectively. The instrument was set to operate at an accelerating voltage of 20 kV, a beam current of 10 nA, and a defocused beam of 5 μm. Counting times were 10 s for the peak and 5 s for the background for each element. The internal ZAF routine was used for data correction (Armstrong 1991).

Backscattered electron (BSE) imaging of wolframite from the different paragenetic stages was conducted at the Advanced Analytical Centre at James Cook University (Townsville, Australia) on carbon-coated polished sections using a high-resolution field emission scanning electron microscope (FE-SEM, Hitachi, SU5000). Backscattered electron images were taken using an acceleration voltage of 20 kV and an emission current of 0.19 mA.

199

200 **Cathodoluminescence microscopy**

201 Cathodoluminescence microscopy (CL) imaging of scheelite was conducted at
202 the Advanced Analytical Centre at James Cook University (Townsville, Australia)
203 using a FE-SEM (Hitachi, SU5000) and a Robinson CL detector and photomultiplier.
204 The SEM-CL analysis was done at 20 kV and an emission current of 0.14 mA using a
205 defocused beam.

206

207 **Laser ablation ICP-MS trace-element analysis**

208 In situ analysis of wolframite and scheelite of the different paragenetic stages
209 was done by using LA-ICP-MS at the Advanced Analytical Centre at James Cook
210 University (Townsville, Australia). Laser ablation was conducted using a Coherent
211 Geolas Pro 193 nm ArF excimer system in helium. Ion-signal intensities were
212 acquired by a Varian 820 quadrupole ICP-MS. Detailed instrument setup conditions
213 are similar as described by Hammerli et al. (2013, 2014). Before analyzing, the
214 ICP-MS was tuned to ensure robust plasma conditions (U/Th sensitivity ratio ~1%)
215 and low oxide production ($ThO^+/Th^+ < 0.3\%$) by using the NIST SRM 610 (Pettke et
216 al. 2012). The homogeneous laser energy density was ~2 J/cm^2 and the repetition rate
217 was 5 Hz. For each analysis, a 30 s background signal was collected before ablation
218 with a duration of 30 s. Helium was used as carrier gas and argon was added as an
219 auxiliary gas. Tungsten (determined by EPMA) was chosen as the internal standard
220 for data reduction. The NIST SRM 610 glass was used as the external standard

This is the peer-reviewed, final accepted version for American Mineralogist, published by the Mineralogical Society of America.
The published version is subject to change. Cite as Authors (Year) Title. American Mineralogist, in press.
DOI: https://doi.org/10.2138/am-2022-8440. http://www.minsocam.org/

(accuracy was verified by analyzing NIST SRM 612), using the reference values of Spandler et al. (2011). GSD, GSE, and NIST SRM 612 glass were used as secondary standards for all elements. The following 45 isotopes were measured in both wolframite and scheelite: ^{7}Li, ^{24}Mg, ^{45}Sc, ^{47}Ti, ^{51}V, ^{53}Cr, ^{55}Mn, ^{57}Fe, ^{59}Co, ^{60}Ni, ^{63}Cu, ^{66}Zn, ^{69}Ga, ^{72}Ge, ^{85}Rb, ^{88}Sr, ^{89}Y, ^{90}Zr, ^{93}Nb, ^{95}Mo, ^{111}Cd, ^{115}In, ^{118}Sn, ^{121}Sb, ^{139}La, ^{140}Ce, ^{141}Pr, ^{146}Nd, ^{147}Sm, ^{153}Eu, ^{157}Gd, ^{159}Tb, ^{163}Dy, ^{165}Ho, ^{166}Er, ^{169}Tm, ^{172}Yb, ^{175}Lu, ^{178}Hf, ^{181}Ta, ^{182}W, ^{208}Pb, ^{209}Bi, ^{232}Th, and ^{238}U. Data processing was performed using the Iolite software (Paton et al. 2011).

Laser ablation ICP-MS trace element mapping of wolframite and scheelite were conducted at the Ore Deposit and Exploration Center of Hefei University of Technology (China), following the procedure described by Wang et al. (2017). An Agilent 7900 ICP-MS equipped with a Photon Machines Analyte HE 193 nm ArF excimer was used for trace element mapping. The He carrier gas was mixed with Ar gas via a T-connector before entering the ICP. The LA ICP-MS mapping was carried out by rastering the laser beam across the sample. The sample was ablated with a beam of 15-20 μm, depending on the grain size, and a scanning speed of 15 μm/s. Ablation was performed using an energy density of 2 J/cm^2 and a laser pulse frequency of 8 Hz. International standard reference materials NIST SRM 610 and GSE-1 were analyzed at the start and the end of each mapping for data calibration. Data processing and images were compiled using the Geochemistry Software V4 (mapping reduction software using MATLAB, Wang et al. 2017; Xiao et al. 2018).

This is the peer-reviewed, final accepted version for American Mineralogist, published by the Mineralogical Society of America.
The published version is subject to change. Cite as Authors (Year) Title. American Mineralogist, in press.
DOI: https://doi.org/10.2138/am-2022-8440. http://www.minsocam.org/

243 **In situ sulfur isotope analysis**

244 Chalcopyrite and pyrite grains intergrown with wolframite and siderite were
245 selected for in situ sulfur isotope analysis. Sulfur stable isotope analysis was
246 conducted at the state Key Laboratory of Geological Processes and Mineral Resources
247 (University of Geosciences Wuhan, China) using a Thermo Scientific Neptune Plus
248 MC-ICP-MS equipped with an NWR FemtoUC femtosecond laser system (New
249 Wave Research, Fremont, CA, U.S.A.). The results are reported in per mil (‰)
250 relative to the Vienna Canyon Diablo Troilite standard (δ^{34}S V-CDT).

251 Helium was used as the carrier gas and mixed with argon (make up gas) after the
252 ablation cell. A spot size of 40 μm, a pulse frequency of 4 Hz and a laser energy
253 density of ~2.5 J/cm^2 were used during single spot ablation. The Neptune Plus was
254 equipped with nine Faraday cups fitted with 10^{11} Ω resistors. The sulfur isotopes (^{32}S,
255 ^{33}S, and ^{34}S) were collected simultaneously (static mode). Details on the method are
256 given by Fu et al. (2017). During the measurements, a pyrite standard sample (PPP-1,
257 $\delta^{34}S_{V\text{-}CDT}$ = 5.40 ± 0.16‰) was used as an external standard to correct the mass
258 fractionation of S isotope for various sulfide samples. In-house references of
259 pyrrhotite (YP136, $\delta^{34}S_{V\text{-}CDT}$ = 1.50 ± 0.30‰) (Li et al. 2019) and chalcopyrite
260 (JGZ-87, $\delta^{34}S_{V\text{-}CDT}$ = 5.50 ± 0.23‰) were analyzed repeatedly as unknown samples in
261 order to verify the accuracy of the calibration method. The accuracy is 0.01–0.15‰
262 for δ^{34}S and 0.11–0.45‰ for δ^{33}S. The precision is 0.16–0.40‰ (2σ) for δ^{34}S and
263 0.35–0.78‰ (2σ) for δ^{33}S. Data processing for LA-MC-ICP-MS analysis was
264 conducted using the ISO-Compass software (Zhang et al. 2020).

This is the peer-reviewed, final accepted version for American Mineralogist, published by the Mineralogical Society of America.
The published version is subject to change. Cite as Authors (Year) Title. American Mineralogist, in press.
DOI: https://doi.org/10.2138/am-2022-8440. http://www.minsocam.org/

265

266 **Whole-rock major and trace elements analysis**

267 Four fresh outcrop and drill-core shale samples were crushed (200 mesh) for
268 whole-rock major and trace elements analysis conducted at the Beijing GeoAnalysis
269 Co. Ltd. Major element analysis on fused glass disks of powdered samples were
270 determined at Beijing GeoAnalysis Co. Ltd using an XRF-1800 X-ray fluorescence
271 spectrometer. Trace elements were also analyzed at Beijing GeoAnalysis Co. Ltd
272 using an Anglient 7500 ICP-MS system on samples that were dissolved at high
273 pressure in Teflon bombs using an HF-HNO_3 mixture (see Wang et al. 2019 for
274 analytical details).

275

276 **TEXTURAL ASPECTS**

277 **Wolframite**

278 Wolframite mainly developed in the quartz-tungstate stage. According to their
279 occurrences (Fig. 4), the shale hosted quartz vein-type wolframites in the Jiaoxi
280 deposit can be divided into four mineralization types (Table 1). Euhedral type I
281 wolframite ($Wol_{S\text{-}I}$) is widely present, intimately associated with euhedral quartz and
282 sericite aggregates, and generally larger than those in other stages (Fig. 4a). Type II
283 wolframite ($Wol_{S\text{-}II}$) is subhedral and intergrown with anhedral quartz (Fig. 4b).
284 Sericite veins are observed along the fractures in subhedral $Wol_{S\text{-}II}$ (Fig. 4c). Type III
285 wolframite ($Wol_{S\text{-}III}$) occurs as sub- to anhedral crystals in between euhedral quartz
286 (Figs. 4d and 4e). Type IV wolframite ($Wol_{S\text{-}IV}$) is relatively rare compared to the

This is the peer-reviewed, final accepted version for American Mineralogist, published by the Mineralogical Society of America.
The published version is subject to change. Cite as Authors (Year) Title. American Mineralogist, in press.
DOI: https://doi.org/10.2138/am-2022-8440. http://www.minsocam.org/

other three wolframite types and occurs as anhedral crystals intergrown with siderite and pyrite (replaced by hematite) (Figs. 4f-4h). It should be noted that $Wol_{S\text{-}IV}$ and $Wol_{S\text{-}I}$ show a distinct different colour in reflected light and that later $Wol_{S\text{-}IV}$ typically developed along the edge or in cracks of subhedral $Wol_{S\text{-}II}$ (Fig. 4f). Early formed wolframites (especially $Wol_{S\text{-}I}$ and $Wol_{S\text{-}II}$) have been altered along the grain boundary or partly replaced by late scheelite (Fig. 4i).

Greisen-type wolframite hosted in BMP and MG can be subdivided into two types (Fig. 5); greisen-type I ($Wol_{G\text{-}I}$) and type II wolframite ($Wol_{G\text{-}II}$). The $Wol_{G\text{-}I}$ develops in quartz veins within the granite and is intergrown with granular pyrite, euhedral quartz, and radial subhedral sericite (Figs. 5a and 5b). Anhedral $Wol_{G\text{-}II}$ is only developed in the greisen (Figs. 5c and 5d).

The different wolframite types show a relatively homogeneous backscattered electron response (Online Materials Figs. OM2a-2d). The $Wol_{S\text{-}IV}$ that developed along the early-formed euhedral $Wol_{S\text{-}I}$ appears darker compared to the $Wol_{S\text{-}I}$ in BSE imaging (Online Materials Fig. OM2c).

Scheelite

Scheelite in the Jiaoxi deposit is rare and only developed in the fluorite stage at depth. According to its occurrence, it can be subdivided into two types, i.e., type I (Sch_I) and type II scheelite (Sch_{II}). Anhedral Sch_I (50-800 μm) replaces early wolframite ($Wol_{S\text{-}I}$ and $Wol_{S\text{-}II}$) and occurs along the wolframite grain boundaries and in fractures (Fig. 4i). These Sch_I grains show a homogeneous CL response (Online

This is the peer-reviewed, final accepted version for American Mineralogist, published by the Mineralogical Society of America.
The published version is subject to change. Cite as Authors (Year) Title. American Mineralogist, in press.
DOI: https://doi.org/10.2138/am-2022-8440. http://www.minsocam.org/

309 Materials Fig. OM2e). Type II scheelite (Sch_{II}, 1-2 mm in size) is larger than Sch_{I} and
310 occurs as sub- to euhedral crystals with concentric growth zones (Online Materials
311 Fig. OM2f).
312
313 ## GEOCHEMISTRY RESULTS
314 ### Composition of wolframite and scheelite
315 #### Major elements
316 Major elements of wolframite and scheelite are given in Online Materials Table
317 OM1. Structural formulae of wolframite and scheelite were calculated based on four
318 oxygens per formula unit.
319 Wolframite has a variable Fe/(Fe+Mn) ratio by mass, which ranges from 0.06 to
320 0.84. Except for $Wol_{S\text{-}IV}$ (0.77-0.84), vein-type wolframite is Mn-enriched
321 (Fe/(Fe+Mn) ratio < 0.5) with compositions close to the hübnerite endmember
322 (Fe/(Fe+Mn) ratio of 0.06 to 0.46). $Wol_{S\text{-}III}$ has the lowest Fe concentration with a
323 Fe/(Fe+Mn) ratio of 0.06-0.09. The Mn concentration in $Wol_{S\text{-}II}$ ranges from 9.8 to
324 14.1 wt. %, which is lower than in $Wol_{S\text{-}I}$ (14.0-15.2 wt.%) (Online Materials Fig.
325 OM3). The highest Mn concentrations (16.5 to 17.9 wt.%) were found in $Wol_{S\text{-}III}$.
326 For the greisen type wolframites, $Wol_{G\text{-}I}$ and $Wol_{G\text{-}II}$ have distinct different Fe
327 and Mn contents. The Fe content in $Wol_{G\text{-}II}$ (11.31-15.54 wt. %) is significantly higher
328 than in $Wol_{G\text{-}I}$ (2.51-5.29 wt. %). The $Wol_{G\text{-}II}$ Fe/(Mn+Fe) ratio ranges from 0.47 to
329 0.78, indicating ferberitic wolframite whereas hübneritic $Wol_{G\text{-}I}$ has a Fe/(Fe+Mn)
330 ratio of 0.10-0.23 (Online Materials Fig. OM3). A positive linear trend can be

This is the peer-reviewed, final accepted version for American Mineralogist, published by the Mineralogical Society of America.
The published version is subject to change. Cite as Authors (Year) Title. American Mineralogist, in press.
DOI: https://doi.org/10.2138/am-2022-8440. http://www.minsocam.org/

observed for Fe/(Mn+Fe) versus W (a.p.f.u.) (Online Materials Fig. OM3). Most wolframite grains, except for the Wol_{S-IV}, have a homogenous Fe-Mn content, which is consistent with the homogenous BSE image (Online Materials Fig. OM2). However, some Wol_{S-I} and Wol_{S-II} grains that are replaced by Wol_{S-IV} show Fe-Mn zonation (Fig. 6). The two different scheelite types show similar major element compositions with WO_3 and CaO contents of 78.7-79.2 and 19.8-20.2 wt. %, respectively.

Trace elements

Trace elements for wolframite and scheelite are given in Online Materials Table OM2. Fe, Mn and Ca were analyzed by EPMA and also by LA-ICP-MS for data quality verification. The results show that LA-ICP-MS data are in good agreement with the EMPA data (Online Materials Fig. OM4), confirming the reliability of the LA-ICP-MS analysis.

Trace element concentrations for different wolframite types are summarized in Online Materials Figure OM5. Wolframite in the Jiaoxi deposit is generally enriched in Mg, Sc, Ti, Cr, Nb, Zr, Sn, and Ta (Online Materials Fig. OM5). Wol_{S-II} and Wol_{G-II} have Mg concentrations of 124-506 ppm and 134-493 ppm, respectively, which are higher than in the other wolframite types (Wol_{S-I}: 57-100 ppm, Wol_{S-III}: 23-43 ppm, Wol_{S-IV}: 37-54 ppm, Wol_{G-I}: 7-27 ppm) (Online Materials Fig. OM5a). The Sc and Sn contents of Wol_{S-I}, Wol_{S-III}, Wol_{S-IV}, and Wol_{G-I} (Sc: 5-119 ppm, Sn: 1-118 ppm) are higher than in Wol_{S-II} (Sc: 2-16 ppm, Sn: < 1-4 ppm) and Wol_{G-II} (Sc: 2-30 ppm, Sn: 1-2 ppm) (Online Materials Fig. OM5b and 5h). BMP hosted greisen-type wolframite have higher Ho, Y, Nb, and Ta contents than the shale-hosted wolframite (Online

This is the peer-reviewed, final accepted version for American Mineralogist, published by the Mineralogical Society of America.
The published version is subject to change. Cite as Authors (Year) Title. American Mineralogist, in press.
DOI: https://doi.org/10.2138/am-2022-8440. http://www.minsocam.org/

353 Materials Fig. OM5e and 5i-5k). All wolframite types show positive trends for Y vs.
354 ΣREE, Zr vs. Hf, Ti vs. Sn, and Sc vs Ti (Figs. 7a-7d). Wol_{S-II} and Wol_{G-II} show higher
355 Mg, Zn, Cr and lower Ti, Sn, Sc, Zr contents than the other wolframite types (Online
356 Materials Fig. OM5). All wolframite types show two distinct trends for Mg vs. Sc,
357 and Zn vs. Sn (Figs. 7e and 7f).

358 Wolframite in the Jiaoxi deposit has variable ΣREE concentrations (< 8715 ppm).
359 Shale-hosted wolframite (5-9 ppm) has relatively lower ΣREE concentrations than the
360 granite-hosted wolframites (5-8715 ppm). The average ΣREE concentration of
361 shale-hosted wolframite decreases from 5 (Wol_{S-I}) to < 1 ppm (Wol_{S-IV}). The ΣREE
362 concentration of Wol_{G-I} (5-13 ppm) is lower than that of Wol_{G-II} (9-8715 ppm). All
363 wolframite types, except for Wol_{G-II}, show HREE enrichment (< 1-19 ppm) compared
364 to LREE (< 1-4 ppm, the LREE content is below the detection limit for most
365 shale-hosted wolframite samples, see Online Materials Table OM2). It is noteworthy
366 that Wol_{G-II} shows a highly variable LREE (1-8650 ppm) content whereas the HREE
367 content (8-65 ppm) is relatively consistent.

368 The REE patterns for all wolframites show a positive Eu anomaly and
369 LREE-HREE fractionating (Figs. 8a-8e). The HREE contents of the greisen-type
370 wolframite (Wol_{G-II} and Wol_{G-I}) are higher than in the MG (Figs. 8b and 8d).

371 Scheelite is enriched in Fe, Mn, Cr, Nb, Sr, Y, and Ta (Online Materials Fig.
372 OM6). Type I scheelite (Sch_I), which replaces wolframite, shows a much higher Fe
373 (870-3800 ppm) and Mn (511-1700 ppm) content than the eu- to subhedral type II
374 scheelite (Sch_{II}, Fe: 141-870 ppm, Mn: 18-411 ppm). Type I scheelite (Sch_I) has a

375 higher La (average value of 83 ppm) and Eu (average value of 27 ppm) content than
376 Sch_{II} (La: 33 ppm, Eu: 10 ppm) (Online Materials Fig. OM6). Sch_I and Sch_{II} show
377 similar Sr (98-779 ppm), Y (22-148 ppm), Na (6-55 ppm), Mg (21- 273 ppm), and Nb
378 (9-25 ppm) contents (Online Materials Table OM2).

379 Compared to wolframite, scheelite has a higher ΣREE content (167-1233 ppm).
380 The Sch_I ΣREE content (170-1233 ppm) is higher than that of Sch_2 (167-636 ppm).
381 Both Sch_I and Sch_{II} show LREE enrichment (59-1080 ppm) relative to HREE (26-153
382 ppm), and a positive Eu anomaly (Fig. 8f).

383 **Minor and trace element maps**

384 Two wolframite grains (ZK2001-200.94 and ZK2001-331.34) showing Fe-Mn
385 zonation were selected for LA-ICP-MS trace element mapping (Fig. 6). Wolframite
386 ZK2001-200.94 shows the textural features typical of $Wol_{S\text{-}IV}$ (Figs. 9b and 9c). The
387 rim composition has higher Fe, Nb, and Ta contents (typical for $Wol_{S\text{-}IV}$) than the core.
388 The core has a higher Mn content than the rim and shows Nb growth zonation similar
389 to $Wol_{S\text{-}I}$ (Fig. 9h). The core and rim are separated from each other by a geochemical
390 transitional zone (Figs. 6b and 10i).

391 Wolframite crystal ZK2001-331.34 exhibits three zones (Online Materials Fig.
392 OM7). The core has higher Mn and Ti contents and shows Nb, Ta, and Sc zonation
393 typical for $Wol_{S\text{-}I}$ (Online Materials Fig. OM7). The core is surrounded by a mantle
394 that shows higher Fe concentrations than the core but is still a Mn-enriched hübnerite,
395 which is typical for $Wol_{S\text{-}II}$. The rim of the crystal has the highest Fe content and
396 higher Sc and Ti but lower Nb and Ta contents than the mantle, which is typical for

This is the peer-reviewed, final accepted version for American Mineralogist, published by the Mineralogical Society of America.
The published version is subject to change. Cite as Authors (Year) Title. American Mineralogist, in press.
DOI: https://doi.org/10.2138/am-2022-8440. http://www.minsocam.org/

397 $Wol_{S\text{-}I}$.

398 One Sch_{II} grain that shows CL zoning (Online Materials Fig. OM2f) was selected
399 for LA-ICP-MS mapping, demonstrating Mg, Li, Sr, Nd, Y, and ΣREE zonation (Fig.
400 10). The Mg and Sr contents decrease whereas the Li, REE, Nd, and Y contents
401 increase from the core to the rim (Fig. 10).

402

403 **Whole-rock chemistry of shale**

404 Shale whole-rock major and trace element data are presented in Online Materials
405 Table OM3. The shale has higher SiO_2 contents (52.3-60.5 wt.%) and similar Al_2O_3,
406 MgO, and total Fe_2O_3 contents compared to other shales in Tibet (Xie et al., 2014).
407 The shale has similar REE contents with PAAS and show a negative Eu anomaly on
408 the chondrite-normalized REE patterns (Fig. 8) (Taylor and McLennan, 1985).

409

410 **Sulfur isotopic compositions**

411 Sulfur isotope compositions of pyrite and chalcopyrite grains are given in Online
412 Materials Table OM4. Chalcopyrite intergrown with siderite (Fig. 11a) shows uniform
413 $\delta^{34}S_{V\text{-}CDT}$ values ranging between +2.07 and +2.30‰ (Figs. 11b and 11c). Pyrite that
414 is intergrown with siderite and chalcopyrite, on the other hand, shows a wide
415 $\delta^{34}S_{V\text{-}CDT}$ range (Fig. 11d) (–31.4 to –2.4‰). Anhedral pyrite that is either intergrown
416 with $Wol_{S\text{-}IV}$ or occurs in between euhedral quartz has $\delta^{34}S_{V\text{-}CDT}$ values ranging from
417 –11.7 to +1.8‰, with most of the $\delta^{34}S_{V\text{-}CDT}$ values ranging between +1.0 and +1.8‰
418 (Figs. 11e and 11f).

419

420 # DISCUSSION

421

422 ## Controls on trace element variations in wolframite and scheelite

423 The chemical compositions of wolframite and scheelite are controlled by the
424 chemical composition of the ore-forming fluid and the crystallochemical effect
425 (Xiong et al. 2017; Harlaux et al. 2018). For example, wolframite HREE enrichment
426 is considered to be controlled by the similar ionic radii of the HREE (Dy^{3+}: 1.07 Å;
427 Lu^{3+}: 0.98 Å), and Fe^{2+} (0.78 Å) and Mn^{2+} (0.83 Å). For scheelite, LREE enrichment
428 is controlled by the similar ionic radii of the LREE (La^{3+}: 1.03 Å; Nd^{3+}: 0.98 Å) and
429 Ca^{2+} (1.0 Å) (ionic radii data are from Shannon, 1976).

430 The very high LREE contents determined in $Wol_{G\text{-}II}$ (three analyses; 8715 ppm,
431 2630 and 176 ppm) (Online Material Table OM2) can be explained by fractures in the
432 wolframite as revealed by BSE imaging. These very high LREE values are not
433 considered in the discussion below.

434 The wolframite and scheelite in the Jiaoxi deposit are characterized by HREE
435 and LREE enrichment, respectively (Fig. 8). It is noteworthy that almost wolframite
436 (except for $Wol_{S\text{-}III}$ and $Wol_{S\text{-}IV}$) and all scheelite types show a large positive Eu
437 anomaly (Eu/Eu* ratios of 0.95-30, Fig. 8), which is different from wolframite and
438 scheelite that are genetically related to highly evolved Eu-depleted granite (Harlaux et
439 al. 2018 and references therein; Zhang et al. 2018; Xiong et al. 2017; Yang et al.
440 2019a). The large positive Eu anomaly of wolframite and scheelite can be explained

441 by: (1) the presence of Eu^{3+} in an oxidized mineralizing fluid due to the similar ionic
442 radius of Eu^{3+} (0.95 Å) and Mn^{2+} (0.83 Å), Fe^{2+} (0.78 Å), and Ca^{2+} (1.0 Å) (Shannon
443 1976; Goldman et al. 2013), or (2) the addition of Eu to the hydrothermal system (Sun
444 and Chen et al. 2017; Li et al. 2018).

445 The scheelite chondrite-normalized Eu concentrations (Eu_N) do not show a
446 correlation with the calculated chondrite-normalized Eu values (Eu_N*, Online
447 Materials Fig. OM8), which indicates a reduced Eu^{2+}-dominated fluid from which
448 scheelite precipitated (Song et al. 2014; Sun and Chen 2017; Li et al. 2018). Reducing
449 conditions are also implied by (1) Raman analysis of primary fluid inclusions hosted
450 in quartz coexisting with wolframite revealed the presence of CH_4 in the mineralizing
451 fluid (Wang et al. 2021a), and (2) the widespread presence of pyrrhotite (Fig. 3d)
452 (Shen et al. 2010; Cao et al. 2014; Sun and Chen 2017). Therefore, the positive Eu
453 anomaly of wolframite and scheelite cannot be explained by an oxidized mineralizing
454 fluid, suggesting that Eu was added. The breakdown of plagioclase during
455 greisenization was a likely source for Eu.

456 Zirconium and Hf are considered to be geochemical twins, i.e. Zr/Hf mass ratios
457 are relatively constant (35-40) in most geological systems (Hoskin and Schaltegger
458 2003). In the Jiaoxi deposit, the greisen type wolframites show a lower Zr/Hf mass
459 ratio (20-27) than the Zr/Hf mass ratio in the shale-hosted wolframite (Wol_{S-I}: 39-50,
460 Wol_{S-II}: 21-78, Wol_{S-III}: 32-44, Wol_{S-IV}: 25-50) (Online Materials Table OM2). A
461 F-B-enriched fluid mobilizes Zr relative to Hf thereby fractionating the element pair
462 (Rubin et al. 1993; Jiang et al. 2005; Cheng et al. 2019). Therefore, the relatively

This is the peer-reviewed, final accepted version for American Mineralogist, published by the Mineralogical Society of America.
The published version is subject to change. Cite as Authors (Year) Title. American Mineralogist, in press.
DOI: https://doi.org/10.2138/am-2022-8440. http://www.minsocam.org/

463 lower Zr/Hf ratio of the greisen type wolframites compared to shale-hosted
464 wolframite indicates that the ore-forming fluid in the greisen stage was enriched in F,
465 which is supported by the presence of abundant fluorite in the greisen ores (Fig. 5b).

466 With regards to the other major and trace elements (e.g., Fe, Mn, Ti, Sc, Mg, Sn,
467 Zr, Nb, and Ta), the different wolframite types have a distinct chemistry. For example,
468 $Wol_{G\text{-}II}$ and $Wol_{S\text{-}II}$ show different Mg, Sc, Sn, and Zn contents compared to $Wol_{G\text{-}I}$,
469 $Wol_{S\text{-}I}$, $Wol_{S\text{-}III}$, and $Wol_{S\text{-}IV}$ (Figs. 7e and 7f). These elements are insensitive to redox
470 conditions (except for Sn), so the variable composition cannot be explained by redox
471 changes. In addition, fluid inclusion and stable isotope studies revealed that
472 wolframite precipitation in the Jiaoxi deposit occurred within a limited temperature
473 range (330-380°C; Wang et al. 2021a). Thus, the chemical variability can also not be
474 explained by temperature changes. Therefore, the variable wolframite chemistry is
475 best explained by the variable chemical composition of the fluid from which
476 wolframite precipitated (Harlaux et al. 2018; Yang et al. 2019a; Xiong et al. 2017).
477

478 **Wolframite and scheelite chemistry as a monitor of fluid evolution**

479 **Fluid-fluid mixing.** All wolframite types show a linear trend for Y vs. ΣREE, Zr
480 vs. Hf, Ti vs. Sn, and Sc vs. Ti (Figs. 7a-7d), which is evidence for (1) a continuous
481 hydrothermal evolution during which these elements were progressively removed
482 from a single fluid phase during mineralization (Korges et al. 2018; Cheng et al.
483 2019), or (2) fluid-fluid mixing (Harlaux et al. 2020; Carocci et al. 2021).

484 The replacement of early Mn-enriched wolframite by late Fe-enriched

This is the peer-reviewed, final accepted version for American Mineralogist, published by the Mineralogical Society of America.
The published version is subject to change. Cite as Authors (Year) Title. American Mineralogist, in press.
DOI: https://doi.org/10.2138/am-2022-8440. http://www.minsocam.org/

485 wolframite (Fig. 4f) indicates that the Fe/(Fe+Mn) ratio increased in the ore-forming
486 fluid (Fig. 6). Trace element mapping shows chemical zoning of wolframite, i.e. the
487 rim has higher HREE, Nb, and Ta contents compared to the core (Fig. 9 and Online
488 Materials Fig. OM7). Therefore, the possibility of a single fluid differentiation model
489 can be excluded as in that scenario the contents of these elements would progressively
490 decrease, which is not the case. Therefore, the chemical variability of wolframite is
491 best explained by a fluid-fluid mixing model.

492 We propose a fluid-fluid mixing model involving a magma-exsolved fluid and a
493 meteoric water. The Nb, Ta, Ti, Sc, Sn, Y, Zr, Hf, Ho, Y, and ΣREE-enriched fluid
494 endmember has the chemical characteristics of a highly evolved granite-derived fluid
495 (Hulsbosch et al. 2016). Mixing of this magmatic fluid with meteoric water induced
496 dilution, which is supported by the linear correlations of Y vs ΣREE, Zr vs. Hf, and Ti
497 vs. Sn (Figs. 7a-7c). The large variation of $\delta^{34}S_{V\text{-}CDT}$ values of pyrite (−31.4 to +1.8‰)
498 intergrown with wolframite and siderite (Fig. 11) is also consistent with mixing of a
499 magmatic fluid with meteoric water (Li et al. 2021). The negative $\delta^{34}S_{V\text{-}CDT}$ values of
500 pyrite implies that S was derived from shale-hosted pyrite suggesting that the
501 meteoric water leached the shale-hosted pyrite during fluid migration (Kohn et al.
502 1998; Lin et al. 2016). This hypothesis is supported by the stable oxygen isotope data
503 of quartz and wolframite, and fluid inclusion data (Wang et al. 2021a).

504 **Leaching metals from coeval granites during the greisenization**

505 Vein-type and greisen-type wolframite show two trends defined by their Mg, Zn,
506 Cr, Ti, and Sn concentrations. The $Wol_{S\text{-}I}$, $Wol_{S\text{-}III}$, $Wol_{S\text{-}IV}$ and $Wol_{G\text{-}I}$ are Sn-Ti-

This is the peer-reviewed, final accepted version for American Mineralogist, published by the Mineralogical Society of America.
The published version is subject to change. Cite as Authors (Year) Title. American Mineralogist, in press.
DOI: https://doi.org/10.2138/am-2022-8440. http://www.minsocam.org/

Sc-enriched and Mg-Zn-depleted, and $Wol_{S\text{-}II}$ and $Wol_{G\text{-}II}$ are Sn-Ti-Zr-Sc-enriched (Figs. 7e and 7f). Enrichment of Sn, Ti, and Sc in wolframite has been reported for numerous quartz vein-type W deposits (Kempe and Wolf 2006; Zhu et al. 2014; Harlaux et al. 2018) which can be explained through coupled substitution (Tindle and Webb 1989):

$$2(Fe, Mn)^{2+} + W^{6+} \leftrightarrow 2Sc^{3+} + (Ti, Sn)^{4+} \quad (1)$$

The positive correlations of Sc vs Ti of wolframite (Fig. 7d) in the Jiaoxi deposit confirm this interpretation. Tin enrichment is generally considered to be inherited from a highly evolved magma through fluid exsolution (Heinrich 1990). As discussed above, the Ti-Sc-enriched fluid represents the magma-exsolved fluid. The lower content of Ti, Sc, and Sn in $Wol_{S\text{-}II}$ and $Wol_{G\text{-}II}$, compared to other wolframite types, may have been caused by a fluid-fluid mixing induced dilution.

Breakdown of plagioclase, K-feldspar, and biotite during greisenization would result in an increase of the pH of the ore-forming fluid causing subsequent wolframite precipitation (Wood and Samson 2000; Hulsbosch et al. 2016; Yang et al. 2019a; Wang et al. 2021a). During greisenization, biotite breakdown would enrich the ore-forming fluid in Mg, Zn, and Fe (Carocci et al. 2021). Due to their similar ionic radii (Shannon 1976), Mg^{2+} (0.72 Å) and Zn^{2+} (0.74 Å) can readily substitute for Fe^{2+} (0.78 Å) and Mn^{2+} (0.83 Å) in wolframite by simple substitution, thus causing the precipitation of Fe-Mg-enriched wolframites (Goldman et al. 2013). This conclusion is supported by the positive correlation of Mg vs. Fe/(Fe+Mn) and Zn vs. Fe/(Fe+Mn) for wolframite (Figs. 12a and 12b). Leaching Fe from biotite during greisenization has

529 also been proposed for the Shimenshi and Xihuashan W deposits (Zhang et al. 2018;
530 Yang et al. 2019a). The breakdown of plagioclase resulted in Eu-enrichment of the
531 fluid, which is reflected in the positive Eu-anomaly of scheelite as discussed
532 previously. Plagioclase breakdown would also release significant Ca into the system,
533 which, in the presence of increasing fluid F content, was removed by the precipitation
534 of fluorite in the greisen (Wang et al., 2021b).

535 Both CL imaging and the element maps show primary oscillatory zoning of Sch_{II}
536 (Fig. 10), which is common for magmatic-related scheelite that precipitated from a
537 hydrothermal fluid with a variable trace element composition (Poulin et al. 2018). The
538 Sch_{II} core has higher Sr and Mg and lower REE, Y, Li, and Nd contents compared to
539 the rim (Fig. 10). Poulin et al. (2018) proposed that the relative enrichment or
540 depletion of Sr in the scheelite may be related to the nature of the ore-forming fluid
541 and that the W-bearing fluid exsolved from a highly fractionated magma is commonly
542 Sr-depleted. Considering that decomposition of biotite, plagioclase, and K-feldspar
543 during greisenization would release Sr, Ca, and Mg into the hydrothermal fluid, we
544 propose that the Sch_{II} core precipitated from a BMP modified-fluid. In conclusion, the
545 decomposition of plagioclase and biotite during the greisenization not only buffered
546 the pH of the magma-exsolved fluid but also released Fe, Zn, Mg Ca, and Eu into the
547 hydrothermal fluid.

This is the peer-reviewed, final accepted version for American Mineralogist, published by the Mineralogical Society of America.
The published version is subject to change. Cite as Authors (Year) Title. American Mineralogist, in press.
DOI: https://doi.org/10.2138/am-2022-8440. http://www.minsocam.org/

548 **Source and nature of Fe in the wolframite.** Numerous sources have been
549 proposed for Fe, including Fe sourced from (1) a highly evolved granite through fluid
550 exsolution (Korges et al., 2018; Harlaux et al. 2018; Yang et al. 2019b), or (2)
551 biotite-bearing granites or metamorphic rocks through fluid-rock interaction
552 (Lecumberri-Sanchez et al. 2017; Zhang et al. 2018). Our data suggest that the Jiaoxi
553 deposit has multiple Fe sources, including the highly evolved MG, the BMP (i.e., Fe
554 released during greisenization), and the shale. The main arguments for this are given
555 below.

556 Michaud and Pichavant (2019) proposed that the Fe/(Fe+Mn) ratio of wolframite
557 can be used as a tracer for the wolframite deposition environment and that
558 Mn-enriched wolframites (hübnerite) mainly precipitate from a Mn-enriched fluid that
559 exsolved from a highly evolved granite. In the Jiaoxi deposit, these early-formed
560 Mn-enriched wolframites (including $Wol_{S\text{-}I}$ and $Wol_{S\text{-}III}$) also indicate that the early
561 ore-forming fluid that exsolved from the highly evolved MG is Mn-enriched. The Mg
562 vs. Fe/(Fe+Mn) and Zn vs. Fe/(Fe+Mn) for wolframite show a positive and a vertical
563 trend (Fig. 12). The positive trend ($Wol_{S\text{-}II}$, $Wol_{G\text{-}I}$, and $Wol_{G\text{-}II}$) indicates that Fe can
564 be leached into the hydrothermal system during greisenization as discussed previously.
565 The vertical trend, on the other hand, shows that a part of Fe ($Wol_{S\text{-}IV}$) is unrelated to
566 greisenization and may be added into the system through other process.

567 Compared to the Mn-enriched cores, the Fe-enriched rim of two wolframite
568 grains shows higher Nb (51-130 ppm), Ta (1-3 ppm), and Ti (70-440 ppm) but lower
569 ΣREE (< 1 ppm), Y (< 1 ppm), and Ho (< 1 ppm) contents (Figs. 6 and 9, and Online

This is the peer-reviewed, final accepted version for American Mineralogist, published by the Mineralogical Society of America.
The published version is subject to change. Cite as Authors (Year) Title. American Mineralogist, in press.
DOI: https://doi.org/10.2138/am-2022-8440. http://www.minsocam.org/

570 Materials Fig. OM7), indicating that the late $Wol_{S\text{-}IV}$ precipitated from a
571 Fe-Nb-Ta-Ti-enriched and ΣREE-Ho-depleted hydrothermal fluid. As discussed above,
572 the low Ho, Y, and ΣREE contents in the fluid are interpreted to result from fluid-fluid
573 mixing induced dilution. In other words, the late $Wol_{S\text{-}IV}$ formed in an open
574 hydrothermal system, in which the meteoric water and the magmatic fluid both have
575 the possibility to carry Fe for the $Wol_{S\text{-}IV}$. If Fe in the late hydrothermal fluid was
576 carried by the magmatic fluid, it may either have been directly sourced from the
577 highly evolved MG and/or leached from the shale during the fluid-rock interaction.

578 Lecumberri-Sanchez et al. (2017) proposed that the wolframite precipitated when
579 an Fe-poor W-bearing fluid interacted with sedimentary rocks and leached Fe from
580 the Fe-enriched shale during muscovitization and tourmalinization. In the Jiaoxi
581 deposit, tourmalinization and muscovitization are absent in the contact zone between
582 quartz veins and shale (Fig. 3c), indicating that the Fe extracted from the shale
583 through fluid-rock interaction was probably limited during the precipitation of the
584 quartz vein-hosted wolframites. In addition, the shale has a high ΣREE (150-180 ppm)
585 and relatively low FeO (< 5 wt.%) content (Online Materials Table OM3), and shows
586 a relatively smooth HREE pattern that is different from $Wol_{S\text{-}IV}$ (Fig. 8e). This also
587 indicates that the contribution of shale-released material into the hydrothermal system
588 is minor (Harlaux et al. 2018). An alternative explanation is that the meteoric water
589 leached Fe from the shales. The extremely negative $\delta^{34}S_{V\text{-}CDT}$ values of pyrite (–31.8
590 to –11.7‰) that is intergrown with wolframite and siderite suggest that sedimentary
591 sulfur derived from shale-hosted pyrite was added to the system (Li et al. 2021). This

592 implies that Fe was leached into the system as a result of the breakdown of
593 shale-hosted pyrite. However, as discussed above, most of the pyrite and chalcopyrite
594 have uniform positive $\delta^{34}S_{V\text{-}CDT}$ values and the $\delta^{34}S_{V\text{-}CDT}$ values increased from –31.4
595 to –2.4‰ in a small area in the pyrite grain (< 200 μm) that is intergrown with
596 chalcopyrite and siderite (Fig. 11d). This observation, together with previous
597 published uniform S isotopic data of galena, sphalerite, pyrrhotite, pyrite, and
598 chalcopyrite in the sulfide stage (+2.6 to +3.7‰, Wang et al. 2021a), suggest that S in
599 the Jiaoxi deposit is dominantly magmatic (i.e., the amount of shale-released S was
600 limited). The precipitation of pyrite, chalcopyrite, galena, pyrrhotite, and sphalerite
601 (Figs. 4g and 11) in the sulfide stage requires a significant amount of Fe. The uniform
602 positive sulfur isotope compositions of these minerals, as discussed above, indicates
603 that the highly evolved MG had the potential to provide sufficient Fe for the quartz
604 vein-type deposit.
605
606 **Implications for ore genesis**
607 The hydrothermal evolution and related ore genesis can be summarized as
608 follows (Fig. 13). During the late crystallization stage of the highly evolved MG, the
609 initial mineralizing fluid was exsolved. High concentrations of F+Cl in the evolving
610 magma lowered the solidus temperature to 400-600°C. Continuous accumulation of
611 hydrothermal fluid induced extensive hydraulic fracturing (Breiter et al. 2017), during
612 which the hydrothermal fluid, enriched in W, Nb, Ta, Mn, and REE, moved up and
613 mixed with meteoric water to form the Mn-enriched $Wol_{S\text{-}I}$ (Figs. 13a and 13b). The

614 residual fluid moved further upward and leached Mg, Zn, Sr, Ca, and Fe from the
615 BMP through the breakdown of biotite, plagioclase, and K-feldspar. The increasing
616 pH values of ore-forming fluid caused local precipitation of Fe-enriched
617 (Fe/(Mn+Fe) > 0.5), greisen-type wolframite (Fig. 13c). Subsequently, this fluid
618 moved upward and mixed with the meteoric water to form $Wol_{S\text{-}II}$, $Wol_{S\text{-}III}$ with
619 relative high Mg and Zn contents. The late Fe-enriched fluid exsolved from the MG
620 moved up and mixed with meteoric water that that carried Fe and S leached from the
621 surrounding shale, to form the Fe-enriched $Wol_{S\text{-}IV}$, siderite, pyrite, and minor
622 chalcopyrite. This Fe-enriched fluid also partly replaced previously wolframite grains
623 along the fractures and edges to form wolframite grains with Fe and Mn zoning (Fig.
624 13b). As temperature decreased and the hydrothermal fluids became depleted in Fe,
625 Mn and F (Wood and Samson 2000; Liu et al. 2021), BMP-derived, Ca-enriched fluid
626 interacted with early-formed wolframite to form Sch_I and the core of Sch_{II}. Finally,
627 the late MG-exsolved REE-Y-enriched fluid moved upward and mixed with the
628 meteoric water to form the Sch_{II} rim with high ΣREE and Y contents (Fig. 13d).

629 These results suggest that the initial ore-forming fluid exsolved from the highly
630 evolved magma of the quartz vein-type tungsten deposit is W- and Mn-enriched.
631 During the fluid evolution, metals such as Fe, Sr, Mg, Zn, and Ca from the
632 surrounding granite and metamorphic rocks were added into the hydrothermal fluid
633 when the system became open. Compared with other quartz vein-type tungsten
634 deposit around the world, such as the Xihuashan in south China, the Nyakabingo, and
635 Bugarama deposits in central Rwanda, and the Argemela mineralized district in

Portugal, several generations of wolframite were observed (Goldmann et al., 2013; Zhang et al., 2018; Michaud and Pichavant, 2019). These different wolframite generations in a deposit commonly show a large variation of Fe/(Mn+Fe) ratios and Mg, Zn, Nb, and Sn contents, which also indicates a dynamic ore-forming environment transitioning with time from a closed to an open hydrothermal system. This study demonstrates that the textural and compositional variations of wolframite and scheelite can be utilized as an optimal proxy to reconstruct the dynamic hydrothermal process of a tungsten deposit.

ACKNOWLEDGMENTS AND FUNDING

This study was financially supported by a grant from the National Key Research & Development Program of China (2021YFC2900100), the Opening Foundation of MNR Key Laboratory of Metallogeny and Mineral Assessment (grant number: ZS2101), the Sichuan Science and Technology Program (2020JDJQ0042), and the Scientific Research Fund of the China Central Non-Commercial Institute (SYSCR2019-03). We would like to thank Mr. Danzhen Wangxiu and Lishen for their assistance in the field, Ms. Liu Mu, Ms. Chen Hongfang, and Dr. Hu Yi for analytical assistance, and Prof. Huang Huiqing for his assistance in data processing. This manuscript greatly benefitted from constructive reviews by Julie Michaud and Iuliu Bobos. Finally, we would like to thank the associate editor Paul Tomascak for his detailed editorial comments.

REFERENCES CITED

Armstrong, J.T. (1991. Quantitative elemental analysis of individual microparticles with electron beam instruments. In K.F.J. Heinrich and D. Newbury, Eds., Electron Probe Quantitation, p. 261-345. Plenum Press, New York.

Audétat, A., Günther, D., and Heinrich, C.A. (2000) Causes for large-scale metal zonation around mineralized plutons: Fluid inclusion LA-ICP-MS evidence from the Mole Granite, Australia. Economic Geology, 95, 1563-1581.

Boynton, W.V. (1984) Cosmochemistry of the rare earth elements: Meteorite studies, in Henderson, P., ed., Rare earth element geochemistry: Amsterdam, Elsevier, p. 63-107.

Brugger, J., Lahaye, Y., Costa, S., Lambert, D., and Bateman, R. (2000) Inhomogeneous distribution of REE in scheelites and the dynamics of Archaean hydrothermal systems (Mt. Charlotte and Drysdale gold deposits, Western Australia). Contributions to Mineralogy and Petrology, 139, 251-264.

Ballouard, C., Poujol, M., Boulvais, P., Branquet, Y., Tartèse, R., and Vigneresse, J.L. (2016) Nb-Ta fractionation in peraluminous granites: a marker of the magmatic-hydrothermal transition. Geology, 44, 231-234.

Breiter, K., Ďurišová, J., Hrstka, T., Korbelová, Z., Vaňková, M.H., Galiová, M.V., Kanický, V., Rambousek, P., Knésl, I., Dobeš, P., and Dosbaba, M. (2017) Assessment of magmatic vs. metasomatic processes in rare-metal granites: A case study of the Cínovec/Zinnwald Sn-W-Li deposit, Central Europe. Lithos, 292, 198-217.

680 Cao, M.J., Qin, K.Z., Li, G.M., Jin L.Y, Evans, N.J., and Yang, X.R. (2014) Baogutu:
681 An example of reduced porphyry Cu deposit in western Junggar. Ore Geology
682 Reviews, 56, 159-180.
683 Cheng, Y.B., Spandler, C., Kemp, A., Mao, J.W., Rusk, B., Hu, Y., and Blake, K.
684 (2019) Controls on cassiterite (SnO_2) crystallization: Evidence from
685 cathodoluminescence, trace-element chemistry, and geochronology at the Gejiu
686 Tin district. American Mineralogist, 104, 118-129.
687 Carocci, E., Marihnac, C., Cathelineau, M., Truche, L., Poujol, M., Boiron, M.C., and
688 Pinto, F. (2021) Incipient wolframite deposition at Panasqueira (Portugal):
689 W-rich rutile and tourmaline compositions as proxies for the early fluid
690 composition. Economic Geology, 116, 123-146.
691 Chicharro, E., Boiron, M.-C., López-G, José Á., Barfod, D.N., and Villaseca, C. (2016)
692 Origin, ore forming fluid evolution and timing of the Logrosán Sn-(W) ore
693 deposits (Central Iberian Zone, Spain). Ore Geology Reviews, 72, 896-913.
694 Ding, L., and Lai, C. (2003) Geologic evidence for preexisting crustal thickening and
695 uplift in the Lhasa terrane before the Indo-Asian collision: Chinese Science
696 Bulletin, 48, 836-842.
697 Fu J.L., Hu Z.C., Li J.W., Yang L., Zhang W., Liu Y.S., Li Q.L., Zong K.Q., and Hu
698 S.H. (2017) Accurate determination of sulfur isotopes ($\delta^{33}S$ and $\delta^{34}S$) in sulfides
699 and elemental sulfur by femtosecond laser ablation MC-ICP-MS with non-matrix
700 matched calibration. Journal of Analytical Atomic Spectrometry, 32, 2341-2351.
701 Goldmann, S., Melcher, F., Gäbler, H.-E., Dewaele, S., De Clercq, F., and Muchez, P.

(2013) Mineralogy and trace element chemistry of ferberite/reinite from tungsten deposits in Central Rwanda. Fortschritte der Mineralogie, 3, 121-144.

Hammerli, J., Rusk, B., Spandler, C., Emsbo, P., and Oliver, N.H.S. (2013) In situ quantification of Br and Cl in minerals and fluid inclusions by LA-ICPMS: A powerful tool to identify fluid sources. Chemical Geology, 337-338, 75-87.

Hammerli, J., Spandler, C., Oliver, N.H.S., and Rusk, B. (2014) Cl/Br of scapolite as a fluid tracer in the earth's crust: Insights into fluid sources in the Mary Kathleen fold belt, Mt. Isa inlier, Australia. Journal Metamorphic Geology, 32, 93-112.

Harlaux, M., Mercadier, J., Marignac, C., Peiffert, C., Cloquet, C., and Cuney, M. (2018) Tracing metal sources in peribatholitic hydrothermal W deposits based on the chemical composition of wolframite: the example of the Variscan French Massif Central. Chemical Geology, 479, 58-85.

Harlaux, M., Kouzmanov, K., Gialli, S., Laurent, O., Andrea, R., Dini, A., Chauvet, A., Menzies, A., Kalinaj, M., and Fontboté, L. (2020) Tourmaline as a tracer of late-magmatic to hydrothermal fluid evolution: the world-class San Rafael Tin (-Copper) deposit, Peru. Economic Geology, 115, 1665-1697.

Hoskin, P.W.O., and Schaltegger, U. (2003) The composition of zircon and igneous and metamorphic petrogenesis. In J.M. Hanchar and P.W.O. Hoskin, Ed., Zircon, 53, p. 27-62. Reviews in Mineralogy and Geochemistry, Mineralogical Society of America, Chantilly, Virginia.

Heinrich, C.A. (1990) The chemistry of hydrothermal tin (-tungsten) ore deposition. Economic Geology, 85, 457-481.

724 Hong, W., Cooke, D.R., Zhang, L., Fox, N., and Thompson, J. (2017) Tourmaline-rich
725 features in the Heemskirk and Pieman Heads granites from western Tasmania,
726 Australia: characteristics, origins, and implications for tin mineralization.
727 American Mineralogist, 102, 876-899.
728 Hou, Z.Q., and Cook, N. (2009) Metallogenesis of the Tibetan collisional orogen: A
729 review. Ore Geology Reviews, 36, 1-24.
730 Hou, Z.Q., Duan, L.F., Lu, Y.J., Zheng, Y.C., Zhu, D.C., Yang, Z.M., Yang, Z.S.,
731 Wang, B.D., Pei, Y.R., Zhao, Z.D., McCuaig, T.C. (2015) Lithospheric
732 architecture of the Lhasa terrane and its control on ore deposits in the
733 Himalayan-Tibetan Orogen. Economic Geology, 110, 1541-1575.
734 Han, J.S., Chen, H.Y., Hong, W., Hollings, P., Chu, G.B., Zhang, L., and Sun, S.Q.
735 (2020) Texture and geochemistry of multi-stage hydrothermal scheelite in the
736 Tongshankou porphyry-skarn Cu-Mo(-W) deposit, estern China: implications for
737 ore-forming process and fluid metasomatism. American Mineralogist, 105,
738 945-954.
739 Hulsbosch, N., Boiron, M.C., Dewaele, S., and Muchez, P. (2016) Fluid fractionation
740 of tungsten during granite-pegmatite differentiation and the metal source of
741 peribatholitic W quartz veins: Evidence from the Karagwe-Ankole belt (Rwanda).
742 Geochimica et Cosmochimica Acta, 175, 299-318.
743 Jiang, S.Y., Chen, W., Zhao, K.D., Zhang, D., Lu, J., and Zhao, H.D. (2021) In situ
744 micro-analysis of isotopic compositions of solid minerals using
745 LA-(MC)-ICP-MS methods and their applications. Journal of Chinese Mass

746 Spectrometry Society, 42, 623-640 (in Chinese with English abstract).

747 Jiang, S.Y., Wang, R.C., Xu, X.S., and Zhao, K.D. (2005) Mobility of high field
748 strength elements (HFSE) in magmatic-, metamorphic-, and
749 submarine-hydrothermal systems. Physics and Chemistry of the Earth, 30,
750 1020-1029.

751 Kapp, P., DeCelles, P.G., Gehrels, G.E., Heizler, M., and Ding, L. (2007) Geological
752 records of the Lhasa–Qiangtang and Indo-Asian collisions in the Nima area of
753 central Tibet. Geological Society of America, Bulletin 119, 917-932.

754 Kapp, P., Murphy, M., Yin, A., Harrison, T.M., Ding, L., and Guo, J. (2003) Mesozoic
755 and Cenozoic tectonic evolution of the Shiquanhe area of western Tibet.
756 Tectonics, 22, 1029.

757 Kapp, P., Yin, A., Harrison, T.M., and Ding, L. (2005) Cretaceous–Tertiary shortening,
758 basin development, and volcanism in central Tibet. GSA Bulletin, 117, 865-878.

759 Kempe, U., and Wolf, D. (2006) Anomalously high Sc contents in ore minerals from
760 Sn–W deposits: possible economic significance and genetic implications. Ore
761 Geology Reviews, 28, 103-122.

762 Korges, M., Weis, P., Lüders, V., and Laurent, O. (2017) Depressurization and boiling
763 of a single magmatic fluid as a mechanism for tin-tungsten deposit formation.
764 Geology, 46, 75-78.

765 Kohn, M.J., Riciputi, L.R., Stakes, D., and Orange, D.L. (1998) Sulfur isotope
766 variability in biogenic pyrite: Reflections of heterogeneous bacterial colonization?
767 American Mineralogist, 83, 1454-1468.

768 Liu, D., Zhao, Z.D., Zhu, D.C., Niu, Y.L., DePaolo, D.J., Harrison, T.M., Mo, X.X.,
769 Dong, G.C., Zhou, S., and Sun, C.G. (2014) Post-collisional potassic and
770 ultrapotassic rocks in southern Tibet: Mantle and crustal origins in response to
771 India-Asia collision and convergence. Geochimica et Cosmochimica Acta,143,
772 207-231.
773 Lecumberri-Sanchez, P., Vieira, R., Heinrich, C.A., Pinto, F., and Wälle, M. (2017)
774 Fluid-rock interaction is decisive for the formation of tungsten deposits. Geology,
775 45, 579-582.
776 Legros, H., Richard, A., Tarantola, A., Kouzmanov, K., Mercadier, J., Vennemann, T.,
777 Marignac, C., Cuney, M., Wang, R.C., Charles, N., Bailly, L., and Lespinasse,
778 M.Y. (2019) Multiple fluids involved in granite-related W-Sn deposits from the
779 world-class Jiangxi province (China). Chemical Geology, 508, 92-115.
780 Li, X.Y., Gao, J.F., Zhang, R.Q., Lu, J.J., Chen, W.H., and Wu, J.W. (2018) Origin of
781 the Muguayuan veinlet-disseminated tungsten deposit, south China: Constraints
782 from in situ trace element analyses of scheelite. Ore Geology Reviews, 99,
783 180-194.
784 Li, R., Xia, X., Yang, S., Chen, H., and Yang, Q. (2019) Off-mount calibration and
785 one new potential pyrrhotite reference material for sulfur isotope measurement
786 by secondary ion mass spectrometry. Geostandards and Geoanalytical Research,
787 43, 177-187.
788 Li, R.C., Chen, H.Y., Wu, N.P., Wang, X.L., and Xia, X.P. (2021) Multiple sulfur
789 isotopes in post-Archean deposits as a potential tracer for fluid mixing processes:

790 An example from an iron oxide–copper–gold (IOCG) deposit in southern Peru.
791 Chemical Geology, 575. 120230.
792 Linnen, R.L., and Williams-Jones, A.E. (1995) Genesis of a magmatic metamorphic
793 hydrothermal system; the Sn-W polymetallic deposits at Pilok, Thailand.
794 Economic Geology, 90, 1148-1166.
795 Lin, Z.Y., Sun, X.M., Peckmann, J., Lu, Y., Xu, L., Strauss, H., Zhou, H.Y., Gong. J.L.,
796 Lu, H.F., and Teichert, B.M.A. (2016) How sulfate-driven anaerobic oxidation of
797 methane affects the sulfur isotopic composition of pyrite: A SIMS study from the
798 South China Sea. Chemical Geology, 440, 26-41.
799 Liu, X.C., Xiao, C.H., and Wang, Y. (2021) The relative solubilities of wolframite and
800 scheelite in hydrothermal fluids: insights from thermodynamic modeling.
801 Chemical Geology, 584, 120488.
802 Mao, J.W., Cheng, Y.B., Chen, M.H., and Franco, P. (2013) Major types and
803 time-space distribution of Mesozoic ore deposits in South China and their
804 geodynamic settings. Mineralium Deposita, 48, 267-294.
805 Michaud, J.A.S., and Pichavant, M. (2019) The H/F ratio as an indictor of contrasted
806 wolframite deposition. Ore Geology Reviews, 104, 266-272.
807 Münker, C., Pfänder, J.A., Weyer, S., Büchl, A., Kleine, T., and Mezger, K. (2003)
808 Evolution of planetary cores and the Earth–Moon system from Nb/Ta
809 systematics. Science, 301, 84-87.
810 Polya, D.A., Foxford, K.A., Stuart, F., Boyce, A., and Fallick, A.E. (2000) Evolution
811 and paragenetic context of low δD hydrothermal fluids from the Panasqueira

W-Sn deposit, Portugal: new evidence from microthermometric, stable isotope, noble gas and halogen analyses of primary fluid inclusions. Geochimica et Cosmochimica Acta, 64, 3357-3371.

Pan, G.T., Wang, L.Q., Li, R.S., Yuan, S.H., Ji, W.H., Yin, F.G., Zhang, W.P., and Wang, B.D. (2012) Tectonic evolution of the Qinghai–Tibet Plateau. Journal of Asian Earth Sciences, 53, 3-14.

Pan, J.Y., Ni, P., and Wang, R.C. (2019) Comparison of fluid processes in coexisting wolframite and quartz from a giant vein-type tungsten deposit, South China: Insights from detailed petrography and LA-ICP-MS analysis of fluid inclusions. American Mineralogist, 104, 1092-1116.

Paton, C., Hellstrom, J., Paul, B., Woodhead, J., and Hergt, J. (2011) Iolite: Freeware for the visualization and processing of mass spectrometric data. Journal of Analytical Atomic Spectometry, 26, 2508.

Pettke, T., Oberli, F., Audétat, A., Guillong, M., Simon, A., Hanley, J.J., and Klemm, L.M. (2012) Recent developments in element concentration and isotope ratio analysis of individual fluid inclusions by laser ablation single and multiple collector ICP-MS. Ore Geology Reviews, 44, 10-38.

Poulin, R.S., Kontak, D.J., McDonald, A., and McClenaghan, M.B. (2018) Assessing scheelite as an ore-deposit discriminator using its trace element and REE chemistry. The Canadian Mineralogist, 56, 265-302.

Rubin, J.N., Henry, C.D., and Price, J.G. (1993) The mobility of zirconium and other immobile elements during hydrothermal alteration. Chemical Geology, 110,

834 29-47.

835 Romer, R.L., and Kroner, U. (2016) Phanerozoic tin and tungsten
836 mineralization-tectonic controls on the distribution of enriched protoliths and
837 heat sources for crustal melting. Gondwana Research, 31, 60-95.

838 Shannon, R.D. (1976) Revised effective ionic radii and systematic studies of
839 interatomic distances in halides and chalcogenides. Acta Crystallographica
840 Section A, 32, 751-767.

841 Shen, P., Shen, Y. C, Wang, J.B., Zhu, H. P, Wang, L, J, and Meng, L. (2010)
842 Methane-rich fluid evolution of the Baogutu porphyry Cu-Mo-Au deposit,
843 Xinjiang, NW China. Chemical Geology, 275, 78-98.

844 Song, G.X., Qin, K.Z., Li, G.M., Evans, N.J., and Chen, L. (2014) Scheelite elemental
845 and isotopic signatures: Implications for the genesis of skarn-type W-Mo
846 deposits in the Chizhou Area, Anhui Province, Eastern China. American
847 Mineralogist, 99, 303-317.

848 Spandler, C., Pettke, T., and Rubatto, D. (2011) Internal and external fluid sources for
849 eclogite-facies veins in the Monviso meta-ophiolite, Western Alps: Implications
850 for fluid flow in subduction zones. Journal of Petrology, 52, 1207-1236.

851 Sun, K.K., and Chen, B. (2017) Trace elements and Sr-Nd isotopes of scheelite:
852 Implications for the W-Cu-Mo polymetallic mineralization of the Shimensi
853 deposit, South China. American Mineralogist, 102, 1114-1128.

854 Tang, J.X., Wang, Q., Yang, C., Ding, S., Lang, X.H., Liu, H.F., Huang, Y., Zheng,
855 W.B., Wang, L.Q., Gao, Y.M., Feng, J., Duan, J.L., Song, Y., Wang, Y.Y., Lin, B.,

Fang, X., Zhang, Z., and Yang, H.H. (2014) Two porphyry-epithermal deposit metallogenic subseries in Tibetan Plateau: Practice of "absence prospecting" deposit metallogenic series. Mineral Deposits, 33, 1151-1170 (in Chinese with English abstract).

Taylor, S.R., and McLennan, S.M. (1985) The continental crust: its composition and evolution, 312 p. Blackwell Scientific Publications, Oxford.

Tindle, A.G., and Webb, P.C. (1989) Niobian wolframite from Glen Gairn in the Eastern highlands of Scotland: A microprobe investigation. Geochimica et Cosmochimica Acta, 53, 1921-1935.

Vindel, E., Lopez, J.A., Boiron, M.C., Cathelineau, M., and Prieto, A.C. (1995) P-V-T-X-fO_2 evolution from wolframite to sulphide depositional stages in intragranitic W-veins. An example from the Spanish Central System. European Journal of Mineralogy, 7, 675-688.

Wang, D.H., Tang, J.X., Ying, L.J., Chen, Z.H., Xu, J.X., Zhang, J.J., Li, S.R., and Zeng, Z.L. (2010) Application of "Five levels + Basement" model for prospecting deposits into depth. Journal of Jilin University (Earth Science Edition), 40, 733-738 (in Chinese with English abstract).

Wang, F.Y., Ge, C., Ning, S.Y., Nie, L.Q., Zhong, G.X., and White, N.C. (2017) A new approach to LA-ICP-MS mapping and application in geology. Acta Petrologica Sinica, 33, 3422-3436.

Wang, L.Q., Wang, Y., Fan, Y., and Danzhen, W.X. (2018) A Miocene tungsten mineralization and its implications in the western Bangong-Nujiang metallogenic

878 belt: Constraints from U-Pb, Ar-Ar, and Re-Os geochronology of the Jiaoxi
879 tungsten deposit, Tibet, China. Ore Geology Reviews, 99, 74-87.
880 Wang, Q., Zhu, D.C., Zhao, Z.D., Liu, S.A., Chung, S.L., Li, S.M., Liu, D., Dai, J.G.,
881 and Wang, L.Q., Mo, X.X. (2014) Origin of the ca. 90 Ma magnesia-rich
882 volcanic rocks in SE Nyima, central Tibet: Products of lithospheric delamination
883 beneath the Lhasa-Qiangtang collision zone. Lithos, 198-199, 24-37.
884 Wang, Y., Juxing T., Liqiang, W., Huizenga, J.M., Santosh, M., Zheng, S.L., Hu, Y.,
885 and Gao, T. (2020) Geology, geochronology and geochemistry of the Miocene
886 Jiaoxi quartz-vein type W deposit in western Lhasa Terrane, Tibet: Implications
887 for ore genesis: Ore Geology Reviews, 120, 103343.
888 Wang, Y., Wang, L.Q., Fan, Y., Li, S., Danzhen, W.X., Zheng, S.L., and Gao, T. (2019)
889 Geological and geochemical characteristics of the Jiaoxi deposit in the western
890 Bangong-Nujiang metallogenic belt, Tibet. Acta Petrologica Sinica, 35, 724-736
891 (in Chinese with English abstract).
892 Wang, Y., Tang, J.X., Wang, L.Q., Huizenga, J.M., and Santosh, M. (2021a)
893 Constraining the genesis of tungsten mineralization in the Jiaoxi deposit, Tibet: A
894 fluid inclusion and H, O, S and Pb isotope investigation. Ore Geology Reviews,
895 139, 10448.
896 Wang, X.S., Williams-Jones, A.E., Hu, R.Z., Shang, L.B., and Bi, X.W., 2021b. The
897 role of fluorine in granite-related hydrothermal tungsten ore genesis: Results of
898 experiments and modeling. Geochimica et Cosmochimica Acta, 292, 170-187.
899 Webster, J., Thomas, R., Förster, H.J., Seltmann, R., and Tappen, C. (2004)

Geochemical evolution of halogen-enriched granite magmas and mineralizing fluids of the Zinnwald tin-tungsten mining district, Erzgebirge, Germany. Mineralium Deposita, 39, 452-472.

Wood, A.A., and Samson, I.M. (2000) The hydrothermal geochemistry in granitoid environments: I. Relative solubilities of ferberite and scheelite as a function of T, P, pH, and mNaCl. Economic Geology, 95, 143-182.

Xie, S.K., Du, B.W., Wang, J., and Dong, Y. (2014) Geochemical characteristics of oil shale member of Dingqinghu Formation in Lunpola Basin of Tibet and their geological implications. Acta Petrologica et Mineralogica, 33, 503-510 (in Chinese with English abstract).

Xiong, Y.Q., Shao, Y.J., Zhou, H.D., Wu, Q.H., Liu, J.P., Wei, H.T., Zhao, R.C., and Cao, J.Y. (2017) Ore-forming mechanism of quartz-vein-type W-Sn deposits of the Xitian district in SE China: implications from the trace element analysis of wolframite and investigation of fluid inclusions. Ore Geology Reviews, 83, 152-173.

Yang, J.H., Zhang, Z., Peng, J.T., Liu, L., and Leng, C.B. (2019a) Metal source and wolframite precipitation process at the Xihuashan tungsten deposit, South China: Insights from mineralogy, fluid inclusion and stable isotope. Ore Geology Reviews, 111, 102965.

Yang J.H., Kang, L.F., Liu, L., Peng, J.T., and Qi, Y.Q. (2019) Tracing the origin of ore-forming fluids in the Piaotang tungsten deposit, South China: Constraints from in-situ analyses of wolframite and individual fluid inclusion. Ore Geology

922 Reviews, 111, 102939.Yang, Z.M., Goldfarb, R., and Chang, Z.S. (2016)
923 Generation of post-collisional porphyry copper deposits in southern Tibet
924 triggered by subduction of the Indian continental plate. Economic Geology, 19,
925 279-300.
926 Yin, A., and Harrison, T.M. (2000) Geologic evolution of the Himalayan-Tibetan
927 orogen. Annual Review of Earth and Planetary Science, 28, 211-280.
928 Zaraisky, G.P., Korzhinskaya, V., and Kotova, N. (2010) Experimental studies of
929 Ta_2O_5 and columbite–tantalite solubility in fluoride solutions from 300 to 550°C
930 and 50 to 100 MPa. Mineralogy and Petrology, 99, 287-30.
931 Zhang, Q., Zhang, R.Q., Gao, J.F., Lu, J.J., and Wu, J.W. (2018) In situ LA-ICP-MS
932 trace element analyses of scheelite and wolframite: Constraints on the genesis of
933 veinlet-disseminated and vein-type tungsten deposits, South China. Ore Geology
934 Reviews, 99, 166-1479.
935 Zhang W., Hu Z.C., and Liu Y.S. (2020) Iso-Compass: new freeware software for
936 isotopic data reduction of LA-MC-ICP-MS. Journal of Analytical Atomic
937 Spectrometry, 35, 1087-1096.
938 Zhao, W.W., Zhou, M.F., Williams-Jones, A.E., and Zhao, Z. (2018) Constraints on
939 the uptake of REE by scheelite in the Baoshan tungsten skarn deposit, South
940 China. Chemical Geology, 477, 123-136.
941 Zhu Y.N., Peng, J.T., Liu, S.Y., and Sun, Y.Z. (2014) Mineral deposit geology and
942 trace element geochemistry of wolframite from the Woxi deposit, western Hunan,
943 China. Geochemica, 43, 287-300 (in Chinese with English abstract).

Zhu, D.C., Li, S.M., Cawood, P.A., Wang, Q., Zhao, Z.D., Liu, S.A., and Wang, L.Q. (2016) Assembly of the Lhasa and Qiangtang terranes in central Tibet by divergent double subduction. Lithos, 245, 7-17.

Zhu, D.C., Pan, G.T., Chung, S.L., Liao, Z.L., Wang, L.Q., and Li, G.M. (2008) SHRIMP zircon age and geochemical constraints on the origin of Lower Jurassic volcanic rocks from the Yeba Formation, southern Gangdese, south Tibet. International Geology Review, 50, 442-471.

Zhu, D.C., Zhao, Z.D., Niu, Y.L., Mo, X.X., Chung, S.L., Hou, Z.Q., Wang, L.Q., and Wu, F.Y. (2011) The Lhasa terrane: record of a microcontinent and its histories of drift and growth. Earth and Planetary Science Letters, 301, 241-255.

955 **Figure captions**

956

957 FIGURE 1. **(a)** Tectonic framework of the northern, southern and central Lhasa
958 subterranes (after Liu et al. 2014), showing the location of Miocene (ultra)potassic
959 rocks and ore deposits including the Jiaoxi deposit in the central Lhasa subterrane. (**b**)
960 Geological sketch map of the Jiaoxi deposit showing the outcrops of the magmatic
961 rocks and stratigraphic units (after Wang et al. 2020). Abbreviations: BNS =
962 Bangong-Nujiang Suture; SNMZ = Shiquan River-Nam Tso Mélange zone; LMF =
963 Luobadui-Milashan fault; KF = Karakorum fault; IYZS = Indus-Yarlung Zangbo
964 Suture. Data from Liu et al. (2014), Yang et al., (2016), and references therein.

965

966 FIGURE 2. Geological map of the Jiaoxi deposit, showing the occurrence of lodes and
967 their relationships with the surrounding rocks (after Wang 2019). The sections A-A'
968 and B-B' can be found on Online materials Figure 1.

969

970 FIGURE 3. Photographs showing representative mineral assemblages and vein
971 crosscutting relationships. (**a-b**) Euhedral wolframite crystals intergrown with quartz
972 and sericite. (**c**) Early quartz-wolframite-sericite vein crosscut by a later quartz-pyrite
973 vein. (**d**) A quartz-pyrrhotite-pyrite vein crosscut by a later fluorite-phengite vein.
974 Abbreviations: Wol = wolframite, Fl = fluorite, Qz = quartz, Ph = phengite, Py =
975 pyrite, Po = pyrrhotite, Ser = sericite.

976

977 FIGURE 4. Reflected light photomicrographs showing the occurrence of different
978 shale-hosted wolframite types. (**a**) Early euhedral Wol_{S-I} intergrown with quartz and
979 sericite assemblages. (**b-c**) Subhedral Wol_{S-II} intergrown with quartz and crosscut by
980 sericite veins. (**d-e**) Anhedral Wol_{S-II} crystal filling the gaps between euhedral quartz
981 crystals. (**f**) Anhedral Wol_{S-II} grain replaced by Wol_{S-IV} along the edge and cracks; (**g**)
982 Anhedral Wol_{S-IV} intergrown with pyrite. (**h**) Anhedral Wol_{S-IV} and siderite filling
983 space among euhedral quartz crystals and replaced by late hematite. (**i**) Early euhedral
984 Wol_{S-I} crystals replaced by late scheelite along the edge. Abbreviations: Wol =
985 wolframite, Qz = quartz, Ph = phengite, Py = pyrite, Po = pyrrhotite, Ser = sericite.
986 Hem = hematite, Sch = scheelite, Sd = siderite.
987
988 FIGURE 5. Photomicrographs showing the greisen type wolframites. (**a** and **b**)
989 Occurrence of Wol_{G-I} intergrown with pyrite, sericite, and quartz (b: cross-polarized
990 light); (**c**) Occurrence of Wol_{G-II}; (d) Anhedral Wol_{G-II} intergrown with sericite and
991 quartz (cross-polarized light).
992
993 FIGURE 6. EPMA traverses of wolframite grains showing contents from cores to rims
994 along (**a**) Reflected light image of Wol_{S-II}. (**b**) Fe and Mn contents from the A (core) to
995 B (rim) in Wol_{S-II}. (**c**) Backscattered electron image of wolframite crystal
996 ZK2001-200.94. (**d**) Fe and Mn contents from C (rim) to D (rim) in wolframite crystal
997 ZK2001-200.94.
998

999 FIGURE 7. Plots of (**a**) Y vs. ΣREE, (**b**) Zr vs. Hf, (**c**) Ti vs. Sn, (**d**) Sc vs. Ti, (**e**) Mg vs.
1000 Sc, and (**f**) Sn vs. Zn for different wolframite types. Positive linear trends can be
1001 observed in (a), (b), (c), and (d). $Wol_{S\text{-}II}$ and $Wol_{G\text{-}II}$ samples have higher Mg and Zn
1002 but lower Sc and Sn contents than the other wolframite types (grey domains in (e) and
1003 (f)).
1004
1005 FIGURE 8. Chondrite-normalized REE patterns of different wolframite and scheelite
1006 types in the Jiaoxi deposit. Chondrite REE values are from Boynton (1984). REE
1007 contents of muscovite granite (MG) are from Wang et al. (2020).
1008
1009 FIGURE 9. BSE image and LA-ICP-MS trace element mapping for wolframite crystal
1010 ZK2001-200.94 (same as in Fig. 6c). (**a**) Homogeneous BSE image. (**b-h**) Trace
1011 element mapping show Fe-Mn-HREE-Sc-Sn-Ti-Nb zonation for wolframite. (**i**)
1012 Schematic diagram for the growth zonation of $Wol_{S\text{-}I}$ and the chemical zonation of
1013 $Wol_{S\text{-}I}$ and $Wol_{S\text{-}IV}$.
1014
1015 FIGURE 10. Cathodoluminescence image and LA-ICP-MS trace element mapping for a
1016 scheelite crystal (Sch_{II}). (**a**) Cathodoluminescence image showing oscillatory zoning.
1017 (**b-g**) Trace element mapping showing primary oscillatory Mg, Li, Nd, Sr, Y, ΣREE
1018 zonation f. (**h**) Schematic diagram showing the chemical zonation of scheelite.
1019

1020 FIGURE 11. In situ sulfur isotope compositions ($\delta^{34}S_{V\text{-}CDT}$ values in per mil) for pyrite
1021 and chalcopyrite intergrown with the Fe-enriched $Wol_{S\text{-}IV}$ and siderite. (**a**)
1022 Chalcopyrite and pyrite intergrown with siderite developed in between euhedral
1023 quartz crystals. (**b**) Sulfur isotope compositions of pyrite showing a large variation in
1024 a small area. (**c** and **d**) Chalcopyrite showing uniform positive sulfur isotope
1025 compositions. (**e** and **f**) Pyrite intergrown with wolframite showing a highly variable
1026 sulfur isotope compositions.
1027
1028 FIGURE 12. Binary plots of (**a**) Mg vs. Fe/(Fe+Mn), (**b**) Zn vs. Fe/(Fe+Mn) showing
1029 positive and vertical trends (grey arrows). The positive trend indicate that a part of Fe
1030 was added into the hydrothermal system with Zn, Mg and Eu during the
1031 greisenization. The vertical trend implies Fe enrichment in the $Wol_{S\text{-}IV}$ that is
1032 unrelated to the greisenization process.
1033
1034 FIGURE 13. (**a**) Schematic representation (not to scale) of hydrothermal evolution and
1035 migration of metals in the Jiaoxi deposit. The brown-red arrows indicate the MG
1036 exsolved fluid comprising the elements W, Mn, Fe, REE, F, S, Nb, Ta, Sn, and Sc. The
1037 green arrows show the MG exsolved fluid leaching Fe, Mg, Zn, Eu, Ca, and Sr from
1038 the BMP. The blue arrows illustrate meteoric water leaching Fe and S from the shale
1039 by. See text for a further discussion of hydrothermal evolution process. (**b**) Sketch
1040 showing the textural and compositional variations of $Wol_{S\text{-}I}$ and $Wol_{S\text{-}IV}$. (**c**) Sketch
1041 showing the location of greisen-type wolframite and their high Fe/(Mn+Fe) ratios (>

1042 0.5). (**d**) Sketch showing the textural and compositional variations of scheelite.
1043 Abbreviations: GP-granite porphyry, MG-muscovite granite, BMP-biotite
1044 monzogranite porphyry.

Online Materials Figure OM1

Simplified geologic cross sections of the Jiaoxi deposit (after Wang et al. 2018). See Fig. 2 for the locations of the cross sections A-A' and B-B'.

Online Materials Figure OM2

High-contrast BSE and CL images of different wolframite and scheelite types. (**a-d**) BSE images showing homogeneous textures of different wolframites types. (**e**) SEM-CL images show anhedral Sch_I crystals with homogeneous textures along the Wol_{S-I}. (**f**) SEM-CL image showing a subhedral Sch_{II} crystal with growth zoning.

Online Materials Figure OM3

Compositional variations of different wolframite types in the Jiaoxi deposit determined by EPMA represented in a W vs. Fe/(Fe+Mn) diagram.

Online Materials Figure OM4

Compositions of Fe and Mn of wolframite in the Jiaoxi deposit determined by EPMA and LA-ICP-MS.

Online Materials Figure OM5

Box-whisker plots for the chemical compositions of different wolframite types. All elemental concentrations are in ppm. The top and bottom of the boxes represent the 25th and 75th percentile of the data and the horizontal lines at the end of the whisker

represent the end of the 1.5 times the interquartile range. The black box represents the mean value.

Online Materials Figure OM6

Box-whisker plots for concentrations (in ppm) of two scheelite types.

Online Materials Figure OM7

Backscattered electron image and LA-ICP-MS trace element mapping for wolframite crystal ZK2001-331.34. (**a**) Backscattered electron image showing a relatively homogeneous texture. (**b-k**) Trace element mapping demonstrating wolframite Fe, Mn, Mg, Ti, Ta, Sc, Mg/Sc, Ti/Cr, Mn/Fe, and Nb zonation. (**l**) Schematic diagram for the chemical zones in crystal ZK2001-331.34.

Online Materials Figure OM8

Chondrite-normalized Eu concentrations (Eu_N) vs. calculated Eu_{CN}* values for scheelites. $Eu_N^* = (Sm_N \times Gd_N)^{1/2}$. The dashed line represents $Eu_N/Eu_N^* = 1$

Table 1 Texture and compositional types of wolframites with typic mineral chemistry

Wolframite type		Textural relations and crystal shape	Mineral Chemistry	Examples
Shale-hosted wolframite	Wol_{S-I}	Widely developed; Associated with euhedral quartz and sericite; Euhedral crystal.	0.20 < Fe/(Fe+Mn) < 0.24; Ti: 418 - 1360 ppm; Sn: 28 - 118 ppm; Mg: 57-100 ppm.	Fig. 4a
	Wol_{S-II}	Intergrown with anhedral quartz; Cross cut by sericite veins; Subhedral crystal.	0.1 < Fe/(Fe+Mn) < 0.4; Ti: 2 - 485 ppm; Sn: 0.5 - 4 ppm; Mg: 124 - 506 ppm.	Fig. 4b-c
	Wol_{S-III}	Sub- to anhedral crystals; Filling in gaps between quartz crystal.	0.06 < Fe/(Fe+Mn) < 0.09; Ti: 6 - 376 ppm; Sn: 0.8 - 37 ppm; Mg: 23 - 43 ppm.	Fig. 4d-e
	Wol_{S-IV}	Relatively rare; Replace the early formed wolframite crystal Anhedral crystal.	0.75 < Fe/(Fe+Mn) < 0.83; Ti: 7 - 376 ppm; Sn: 1.6 - 19 ppm; Mg: 37 - 54 ppm.	Fig. 4f-h
Greisen-hosted wolframite	Wol_{G-I}	Develops in quartz veins within the granite; Intergrown with granular pyrite, euhedral quartz, and sericite; Subhedral crystal.	0.1 < Fe/(Fe+Mn) < 0.2; Ti: 14 - 36 ppm; Sn: 2 - 12 ppm; Mg: 7 - 27 ppm.	Fig. 5a-b
	Wol_{G-II}	Only develops in the greisen; Anhedral crystal; Grain size <500 μm.	0.47 < Fe/(Fe+Mn) < 0.78; Ti: 22 - 219 ppm; Sn: 1.3 - 2.4 ppm; Mg: 134 - 493 ppm.	Fig. 5c-d

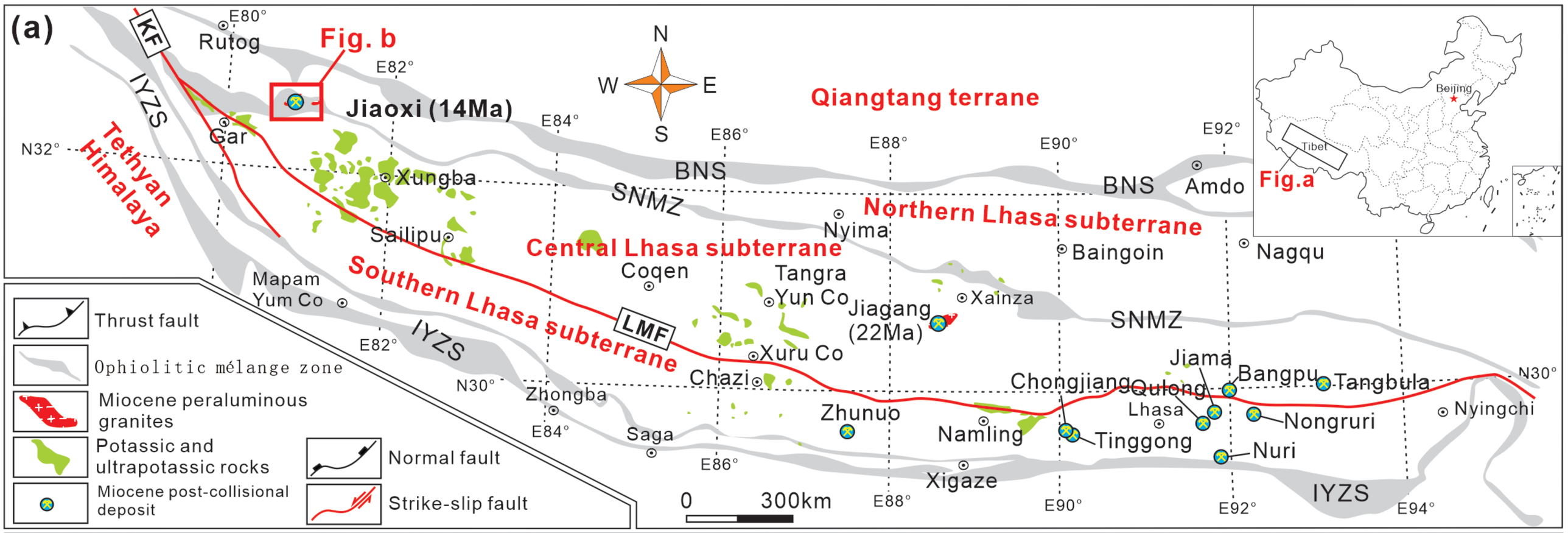
(a)
KF
IYZS
Tethyan Himalaya
Fig. b
Rutog
Gar
Jiaoxi (14Ma)
Xungba
Sailipu
Mapam Yum Co
Southern Lhasa subterrane
Central Lhasa subterrane
Northern Lhasa subterrane
Qiangtang terrane
BNS
SNMZ
LMF
Coqen
Tangra Yun Co
Nyima
Baingoin
Amdo
Nagqu
Jiagang (22Ma)
Xainza
Xuru Co
Chazi
Zhongba
Saga
Zhunuo
Namling
Xigaze
Chongjiang
Qulong
Jiama
Bangpu
Tangbula
Lhasa
Tinggong
Nuri
Nongruri
Nyingchi
Beijing
Tibet
Fig.a
N
S
W
E
E80°
E82°
E84°
E86°
E88°
E90°
E92°
E94°
N32°
N30°
0 300km
Thrust fault
Ophiolitic mélange zone
Miocene peraluminous granites
Potassic and ultrapotassic rocks
Miocene post-collisional deposit
Normal fault
Strike-slip fault

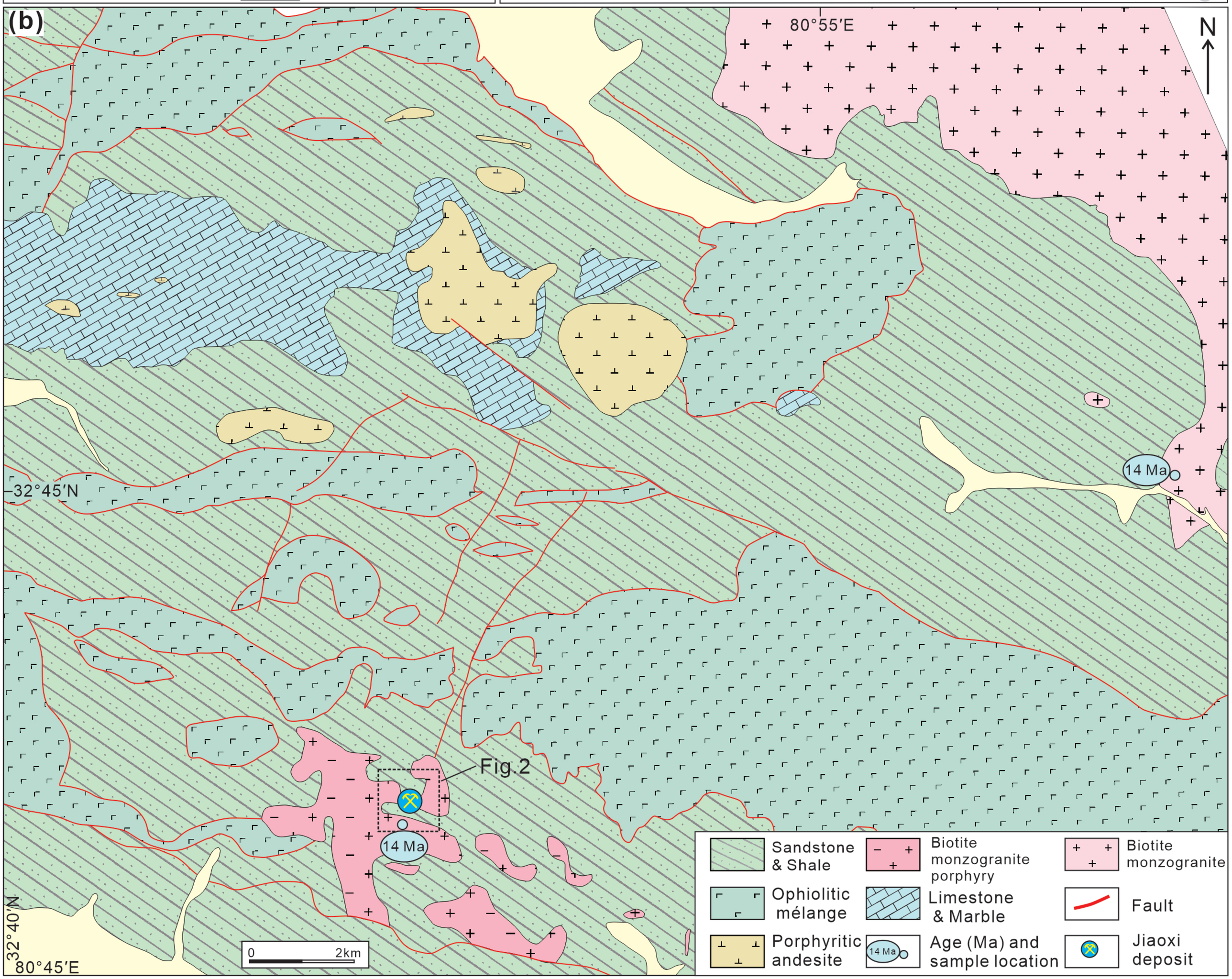
(b)
80°55′E
32°45′N
32°40′N
80°45′E
14 Ma
Fig.2
0 2km
Sandstone & Shale
Ophiolitic mélange
Porphyritic andesite
Biotite monzogranite porphyry
Limestone & Marble
Age (Ma) and sample location
Biotite monzogranite
Fault
Jiaoxi deposit

Figure 1

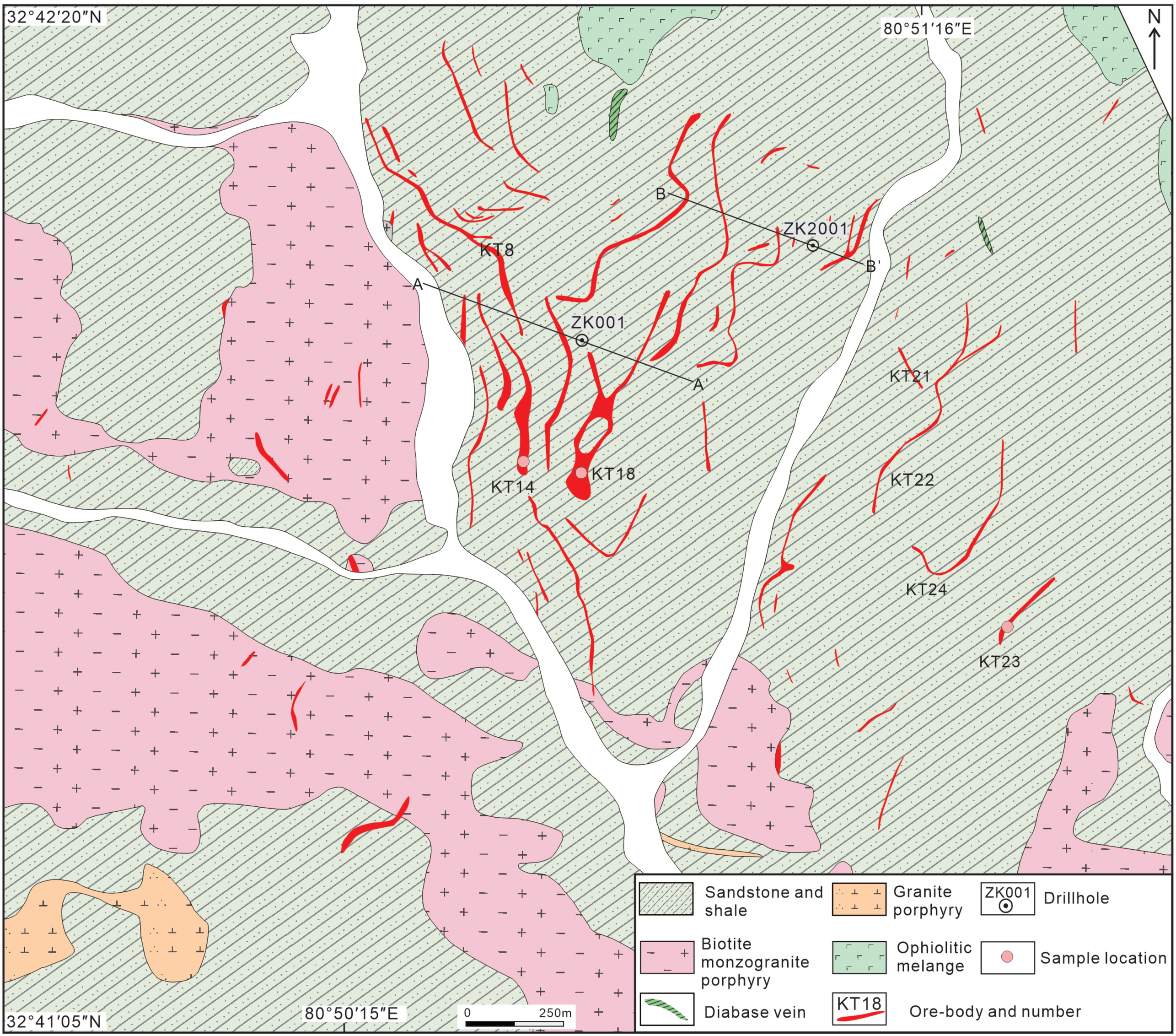
32°42′20″N
80°51′16″E
N
B
B'
ZK2001
KT8
A
A'
ZK001
KT21
KT14
KT18
KT22
KT24
KT23
Sandstone and shale
Granite porphyry
ZK001
Drillhole
Biotite monzogranite porphyry
Ophiolitic melange
Sample location
Diabase vein
KT18
Ore-body and number
32°41′05″N
80°50′15″E
0
250m

Figure 2

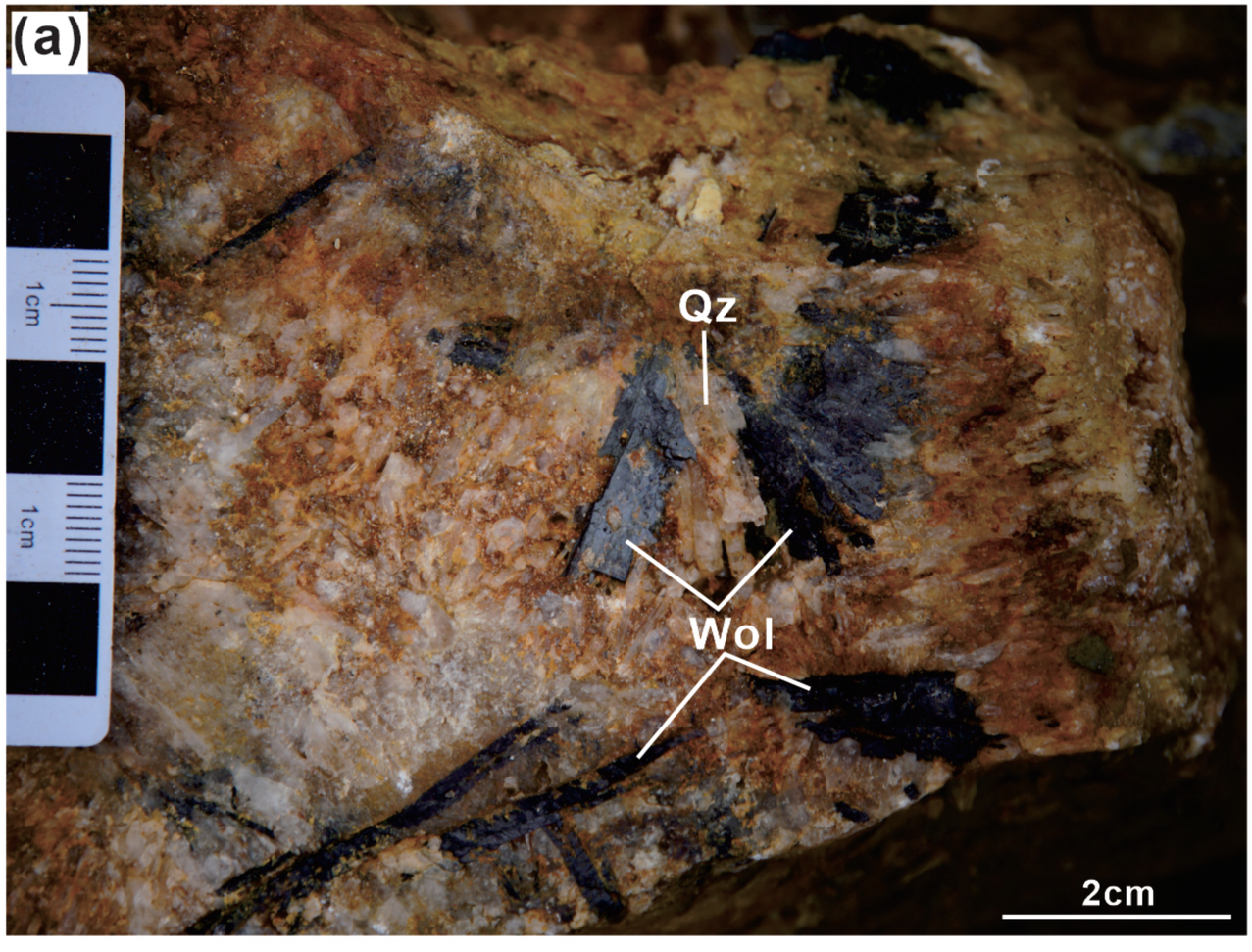
(a)
1cm
1cm
Qz
Wol
2cm

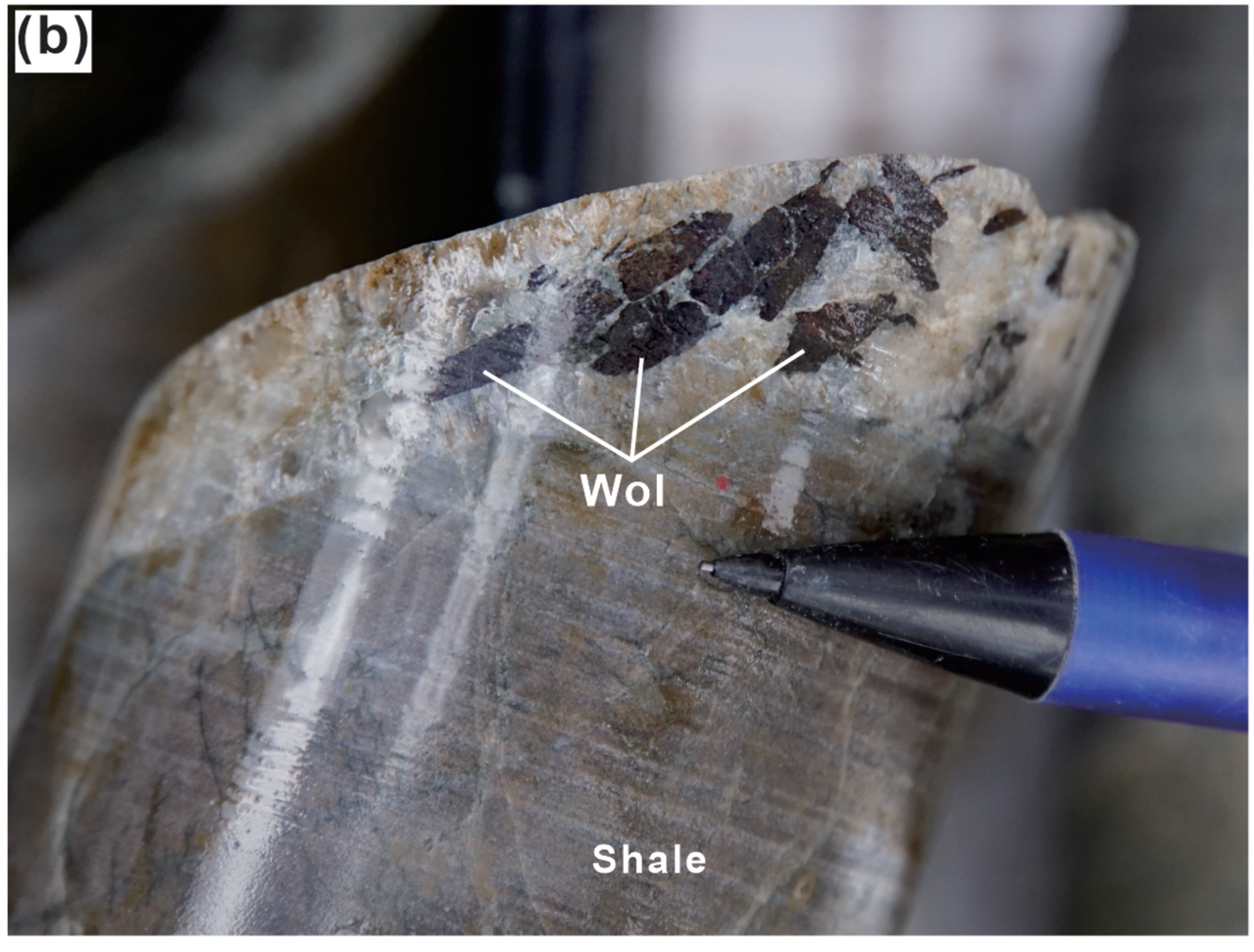
(b)
Wol
Shale

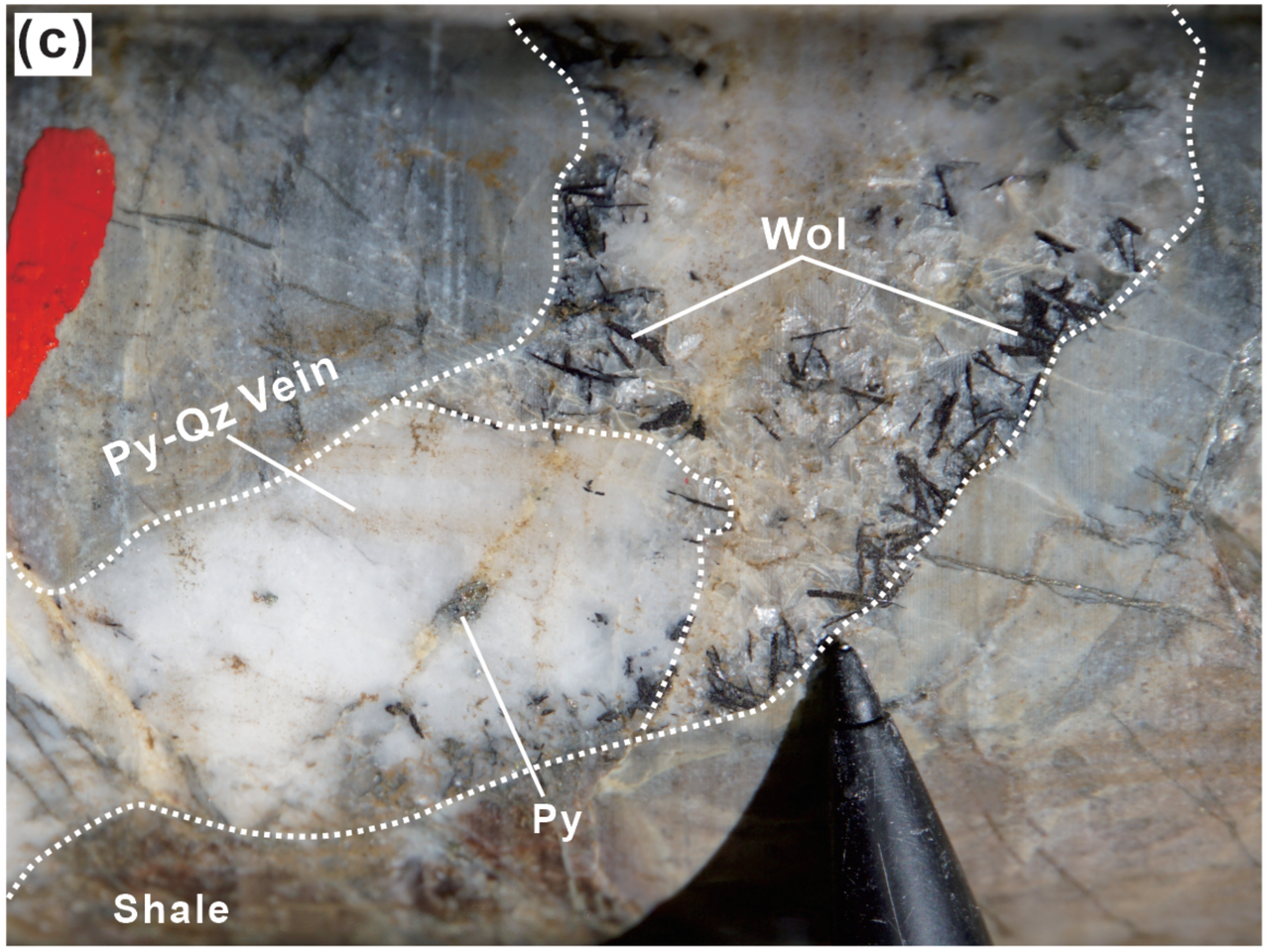
(c)
Wol
Py-Qz Vein
Py
Shale

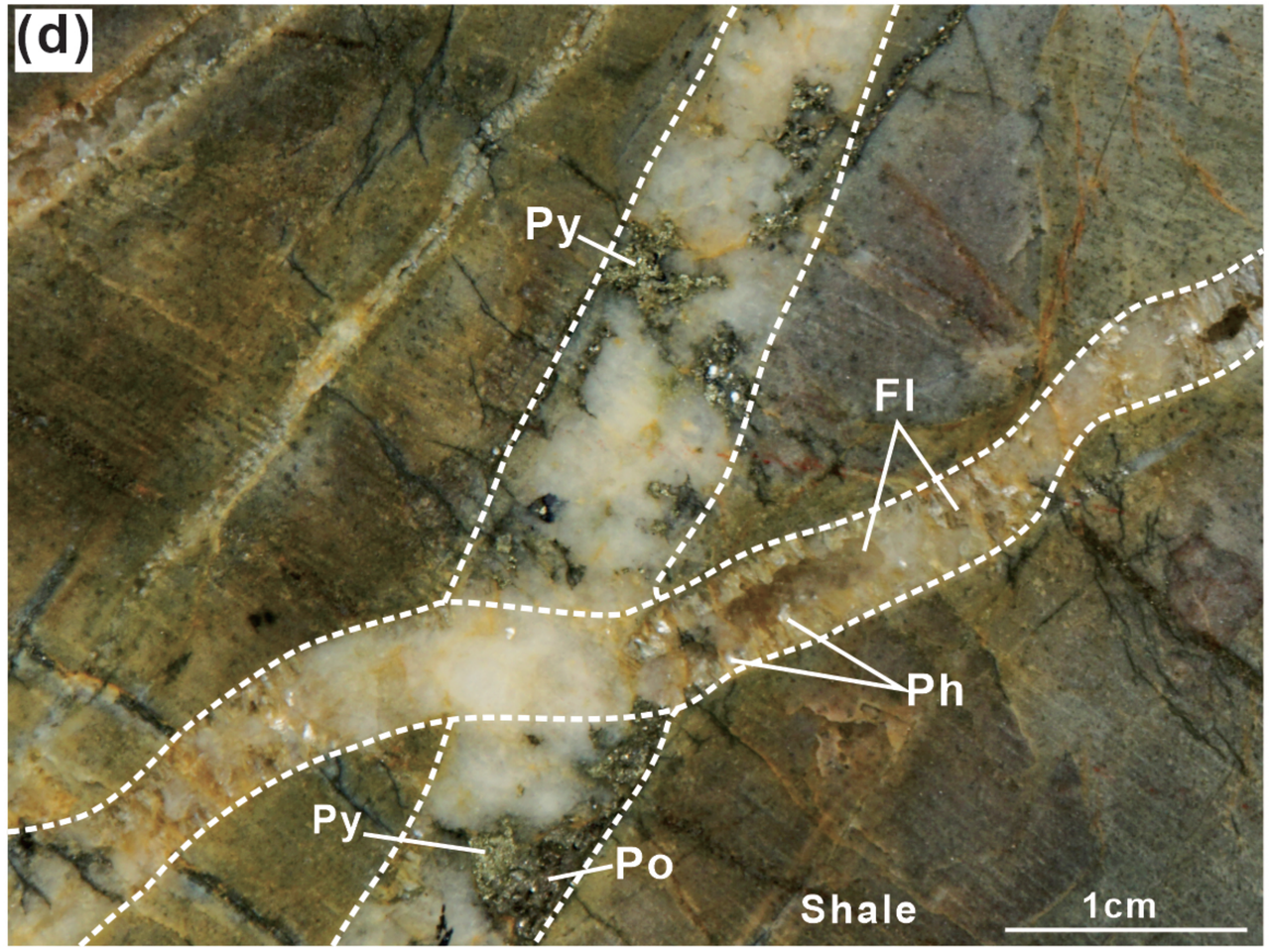
(d)
Py
Fl
Ph
Py
Po
Shale
1cm

Figure 3

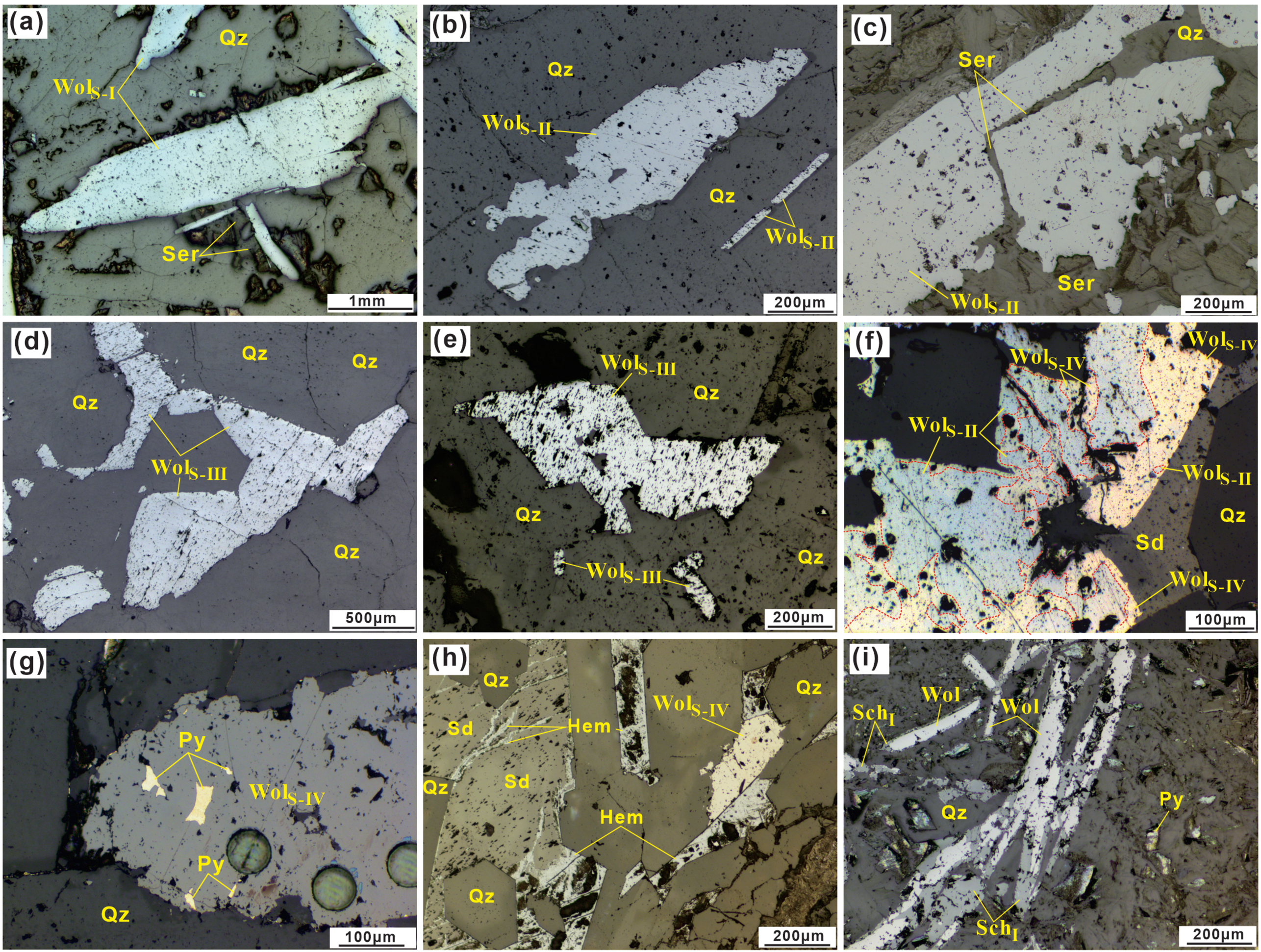
(a)
Qz
Wol S-I
Ser
1mm
(b)
Qz
Wol S-II
Qz
Wol S-II
200μm
(c)
Qz
Ser
Ser
Wol S-II
200μm
(d)
Qz
Qz
Qz
Wol S-III
Qz
500μm
(e)
Wol S-III
Qz
Qz
Wol S-III
200μm
(f)
Wol S-IV
Wol S-IV
Wol S-II
Wol S-II
Qz
Sd
Wol S-IV
100μm
(g)
Py
Wol S-IV
Py
Qz
100μm
(h)
Qz
Qz
Sd
Hem
Wol S-IV
Qz
Sd
Hem
Qz
200μm
(i)
Sch I
Wol
Wol
Qz
Py
Sch I
200μm

Figure 4

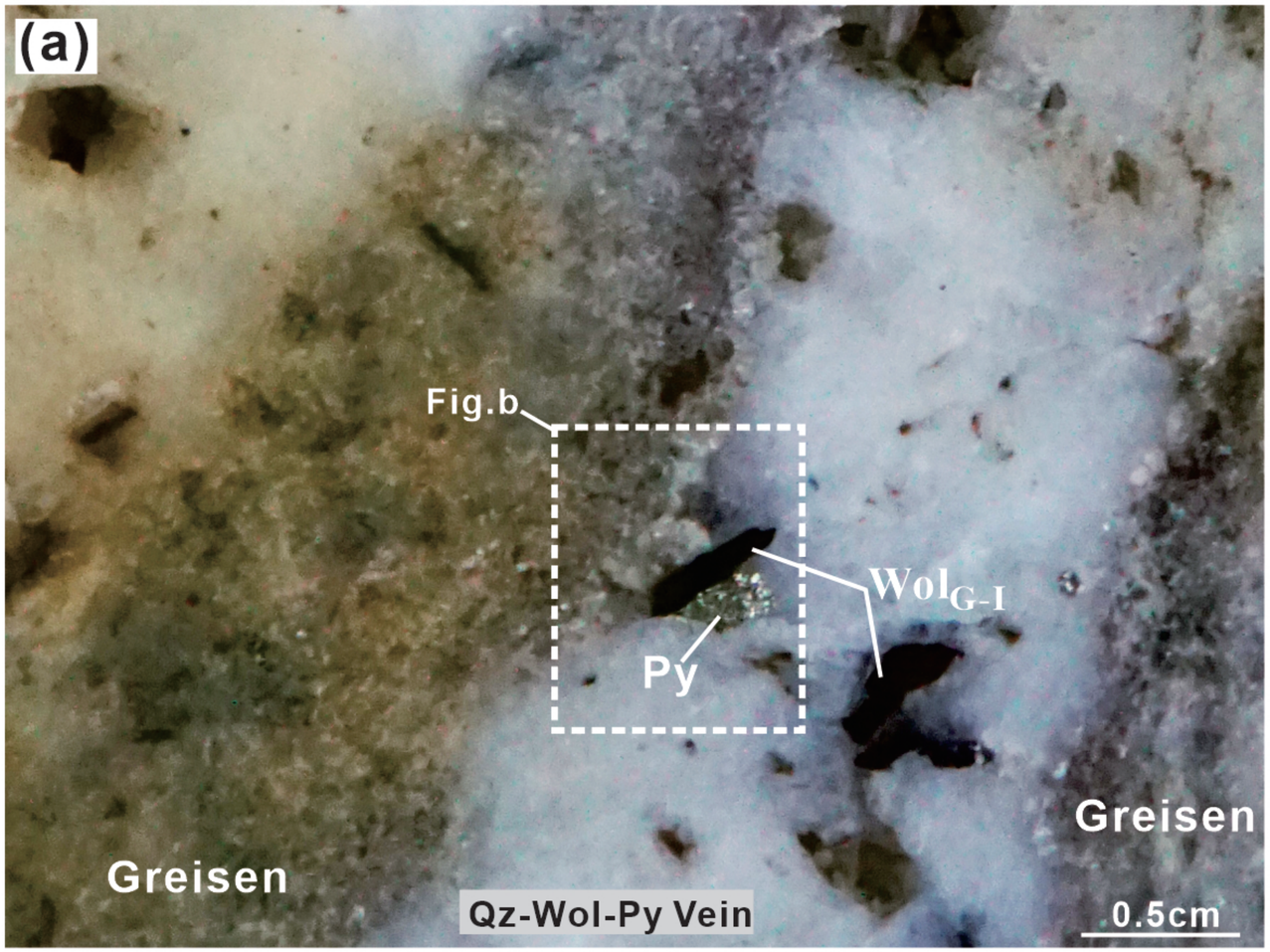
(a)
Fig.b
Py
Wol$_{G-I}$
Greisen
Greisen
Qz-Wol-Py Vein
0.5cm

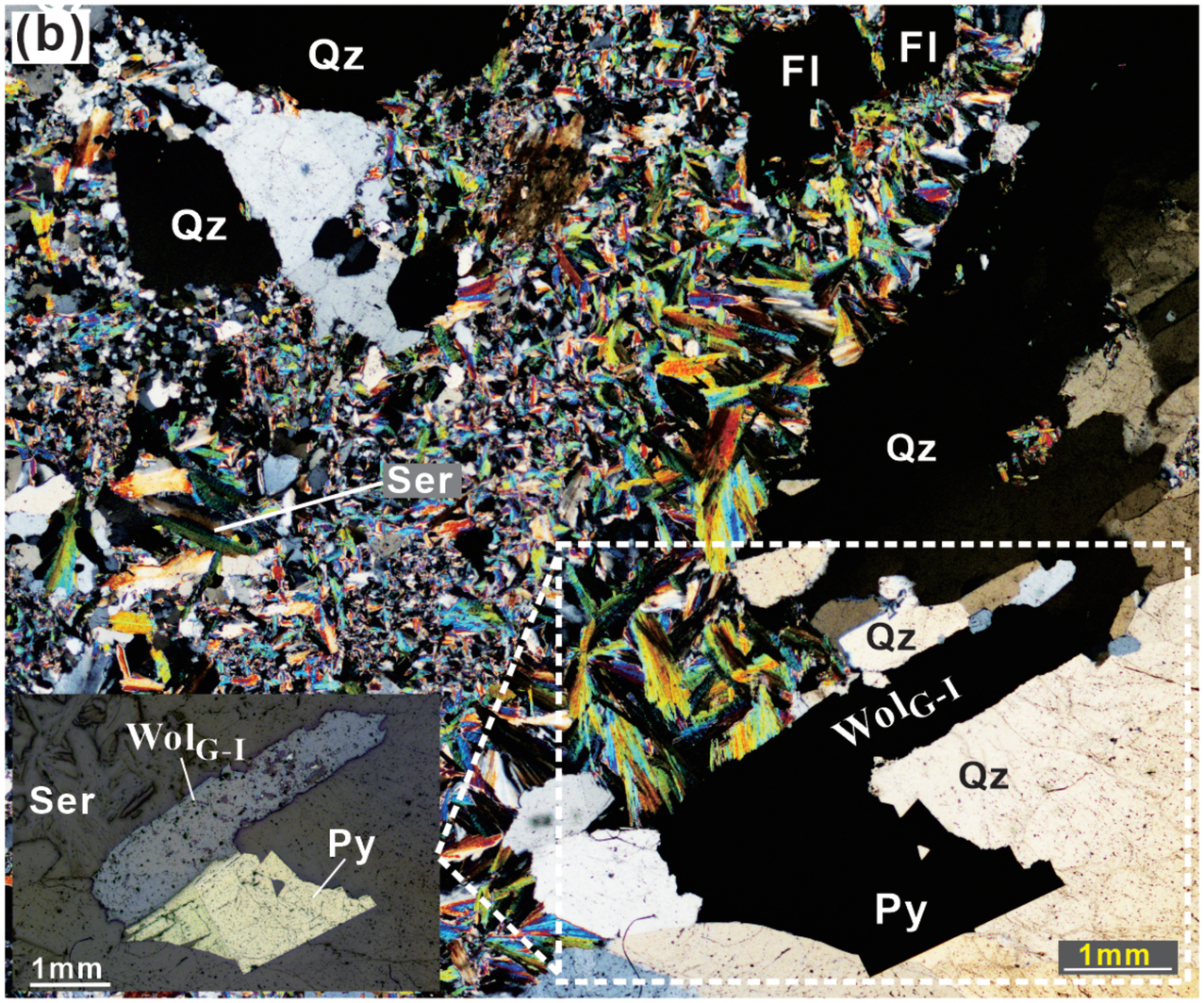
(b)
Qz
Fl
Fl
Qz
Qz
Ser
Qz
Wol$_{G-I}$
Qz
Py
1mm
Wol$_{G-I}$
Ser
Py
1mm

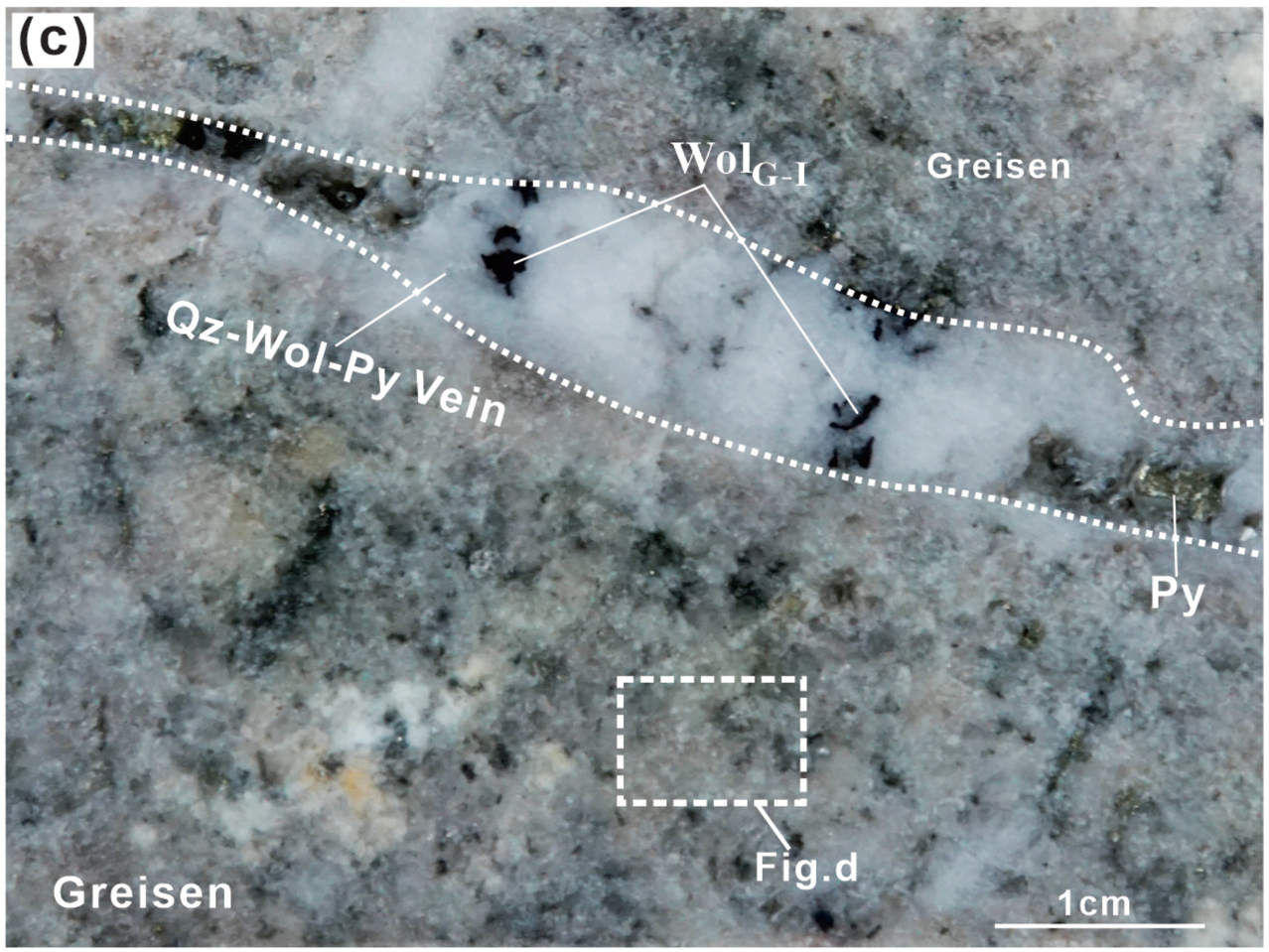
(c)
Wol$_{G-I}$
Greisen
Qz-Wol-Py Vein
Py
Fig.d
Greisen
1cm

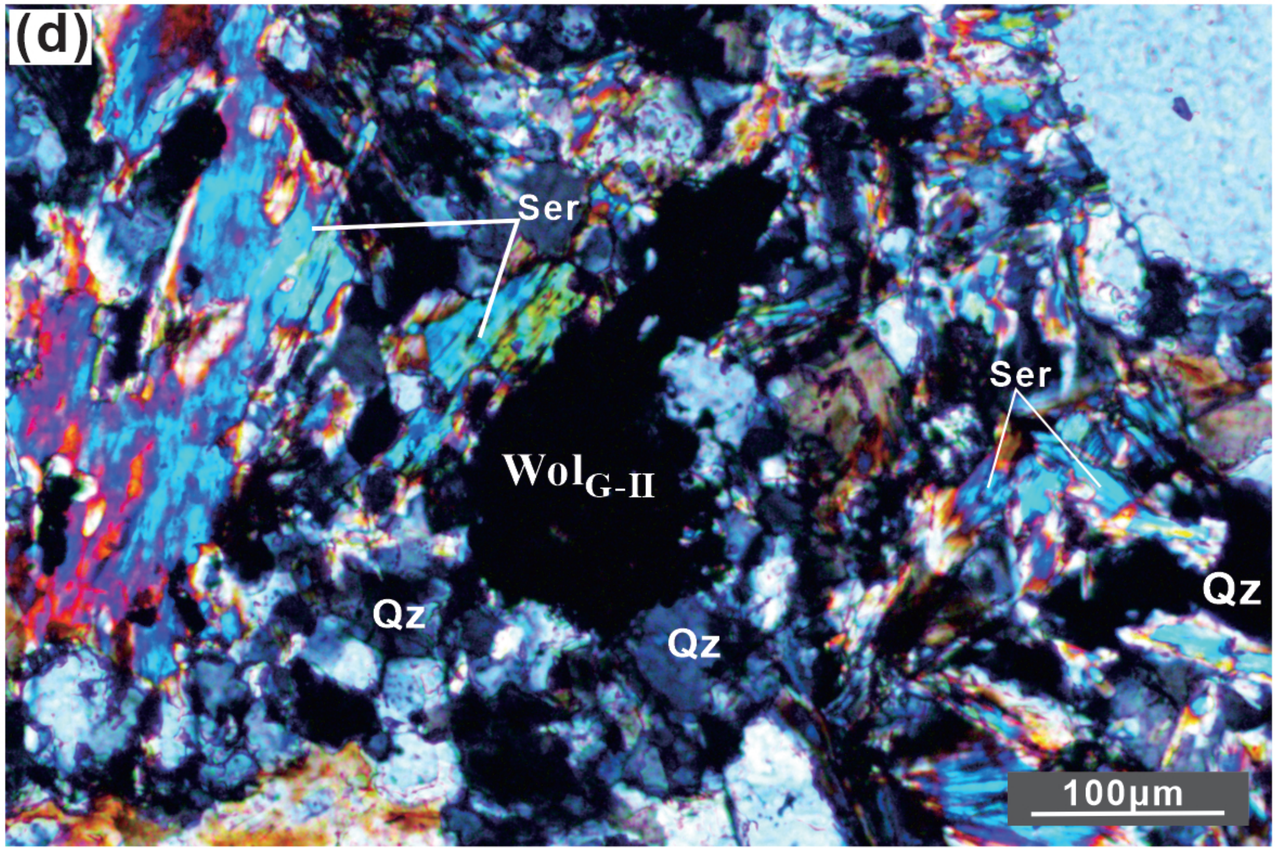
(d)
Ser
Ser
Wol$_{G-II}$
Qz
Qz
Qz
100μm

Figure 5

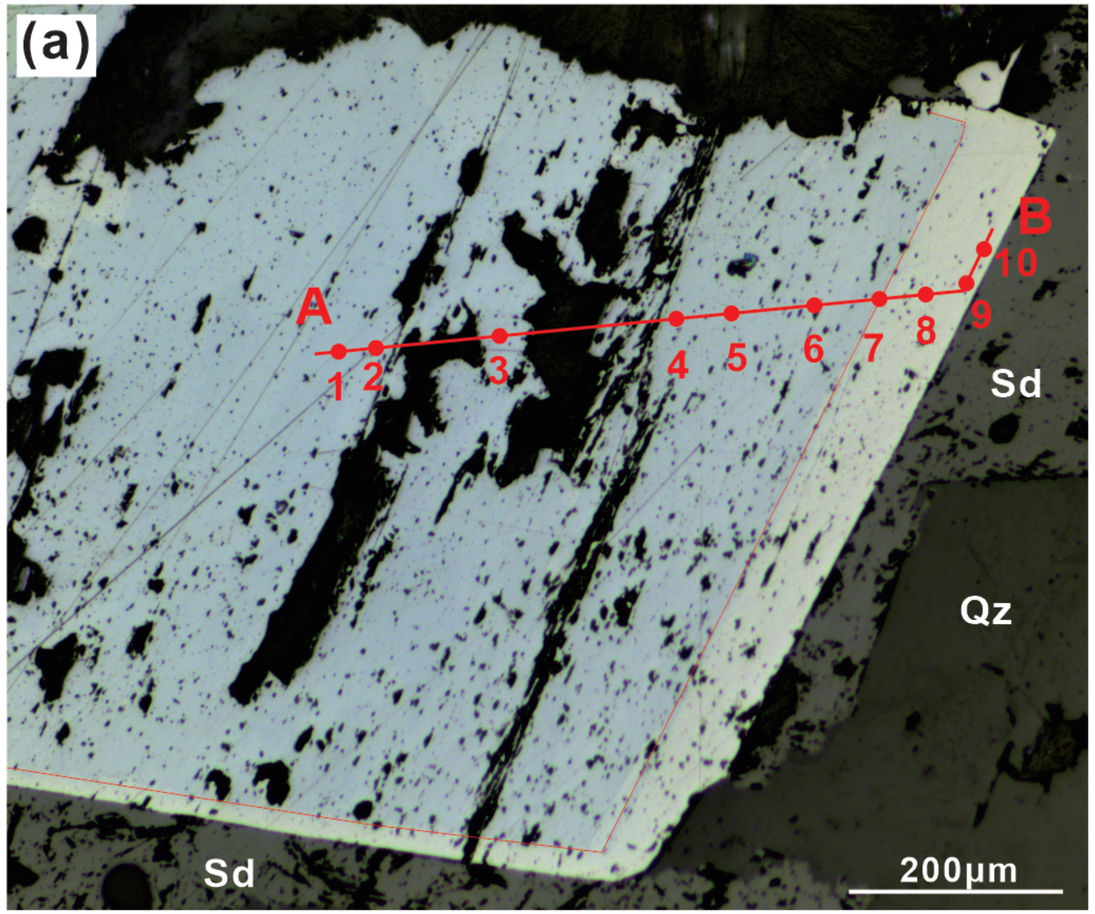
(a)
A
B
1
2
3
4
5
6
7
8
9
10
Sd
Qz
Sd
200μm

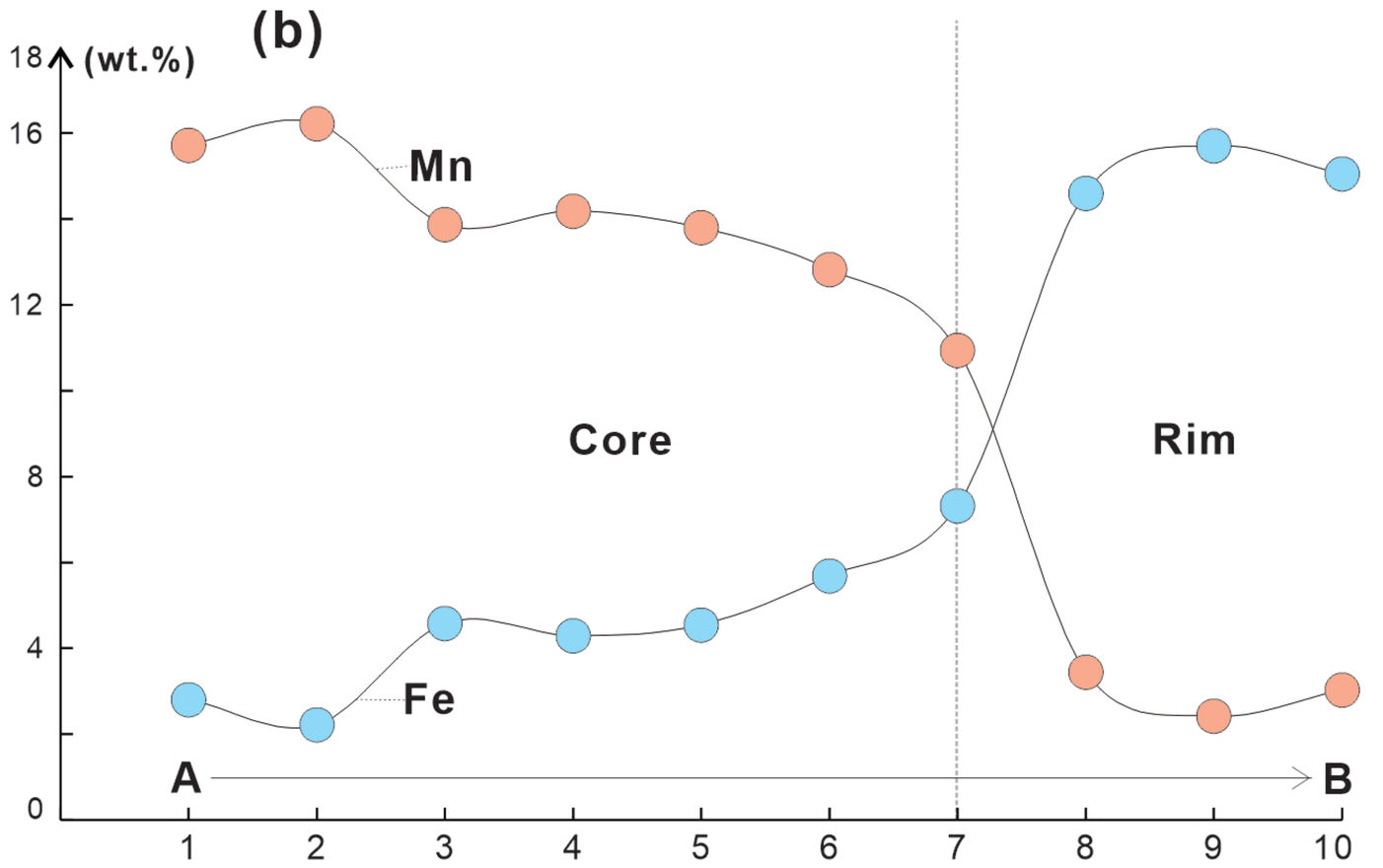
(b)
18
(wt.%)
16
12
8
4
0
Mn
Fe
Core
Rim
A
B
1
2
3
4
5
6
7
8
9
10

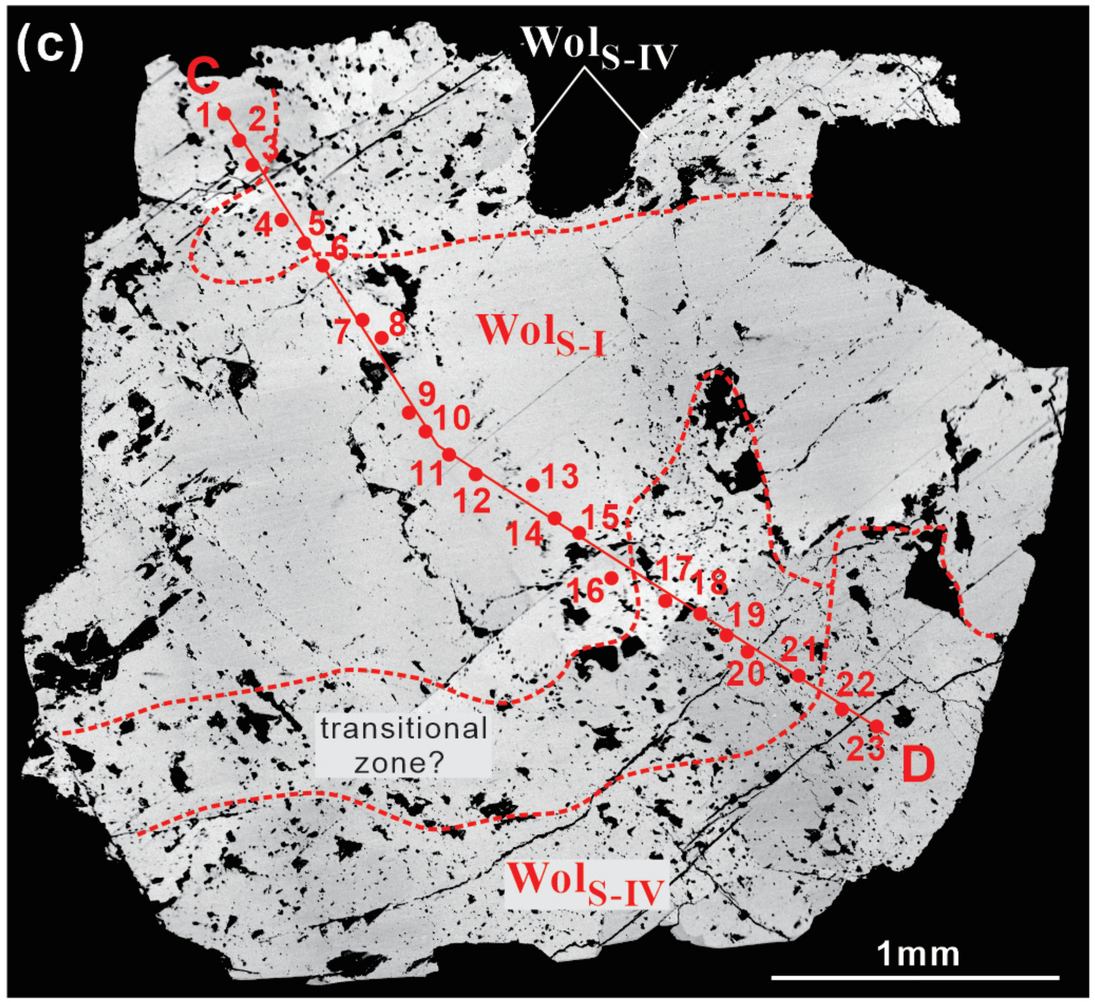
(c)
C
D
Wol S-IV
Wol S-I
Wol S-IV
transitional zone?
1mm

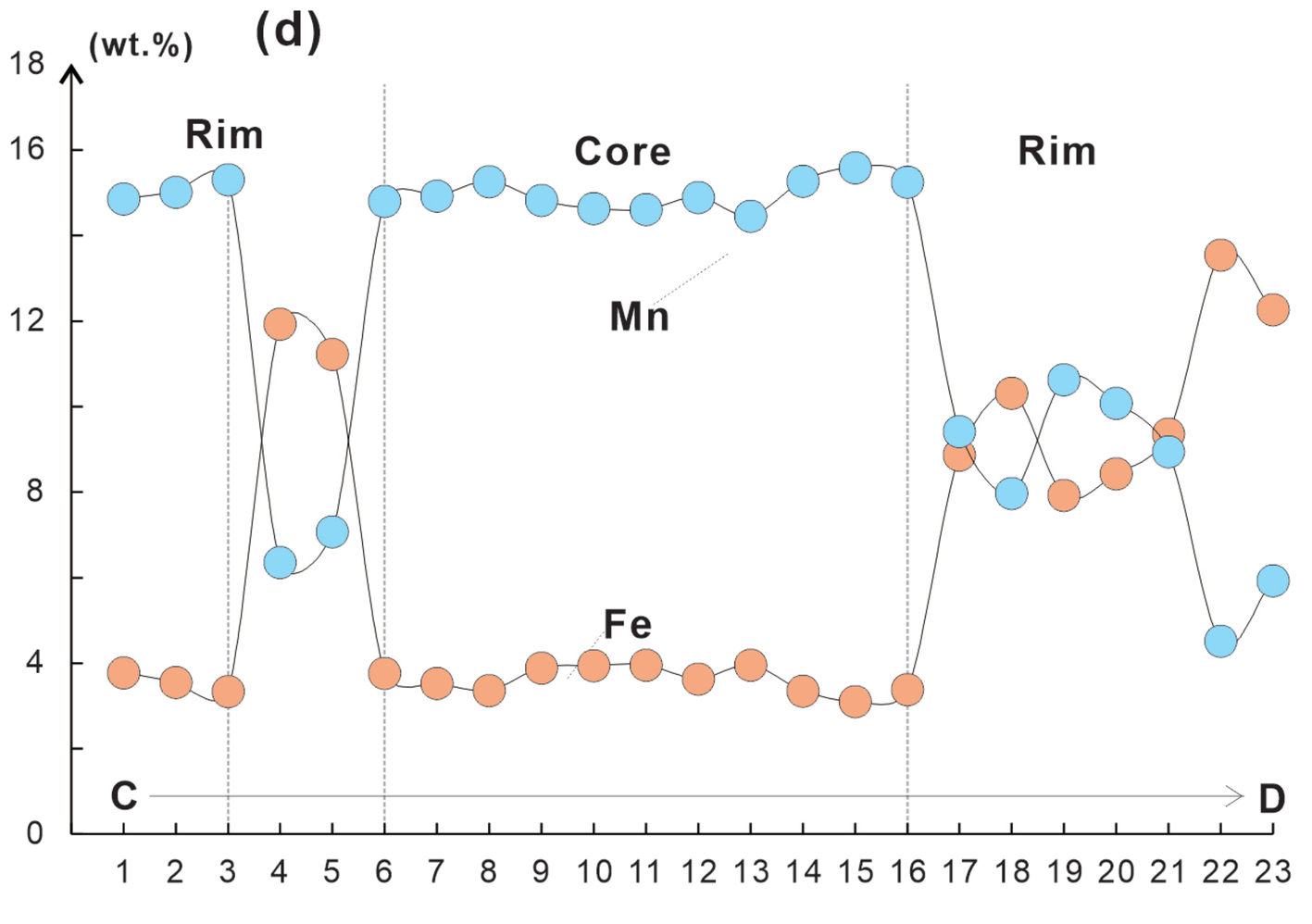
(d)
(wt.%)
18
16
12
8
4
0
Rim
Core
Rim
Mn
Fe
C
D
1 2 3 4 5 6 7 8 9 10 11 12 13 14 15 16 17 18 19 20 21 22 23

Figure 6

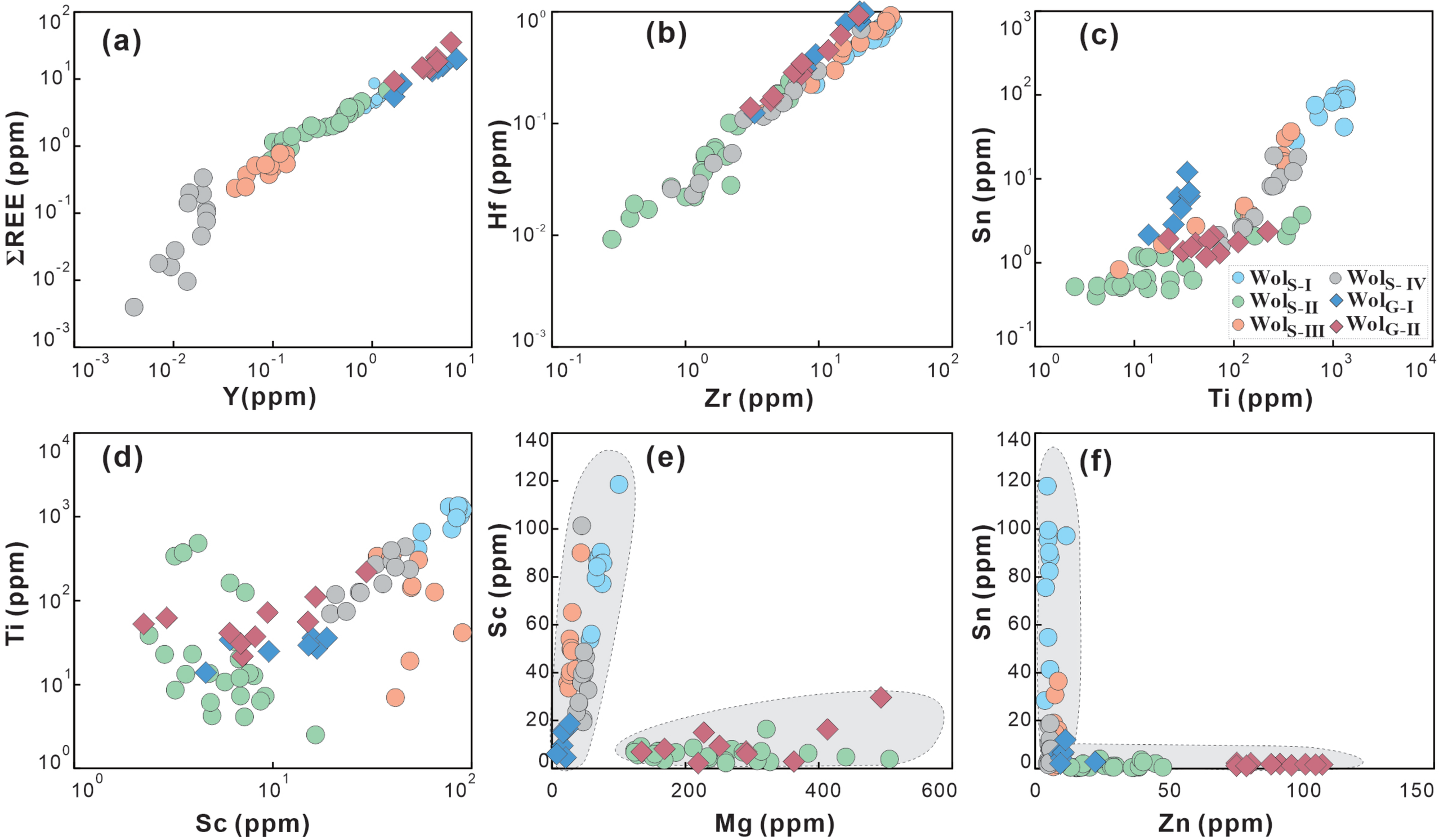
(a)
ΣREE (ppm)
Y(ppm)
(b)
Hf (ppm)
Zr (ppm)
(c)
Sn (ppm)
Ti (ppm)
Wol S-I
Wol S-II
Wol S-III
Wol S- IV
Wol G-I
Wol G-II
(d)
Ti (ppm)
Sc (ppm)
(e)
Sc (ppm)
Mg (ppm)
(f)
Sn (ppm)
Zn (ppm)

Figure 7

(a)

Wol_{S-I}

(b)

Wol_{G-I}

(c)

Wol_{S-II}

(d)

Wol_{G-II}

(e)

Wol_{S-III} & Wol_{S-IV}

(f)

Sch_I & Sch_{II}

Sample/Chondrite

La Ce Pr Pm Nd Sm Eu Gd Tb Dy Ho Er Tm Yb Lu

Figure 8

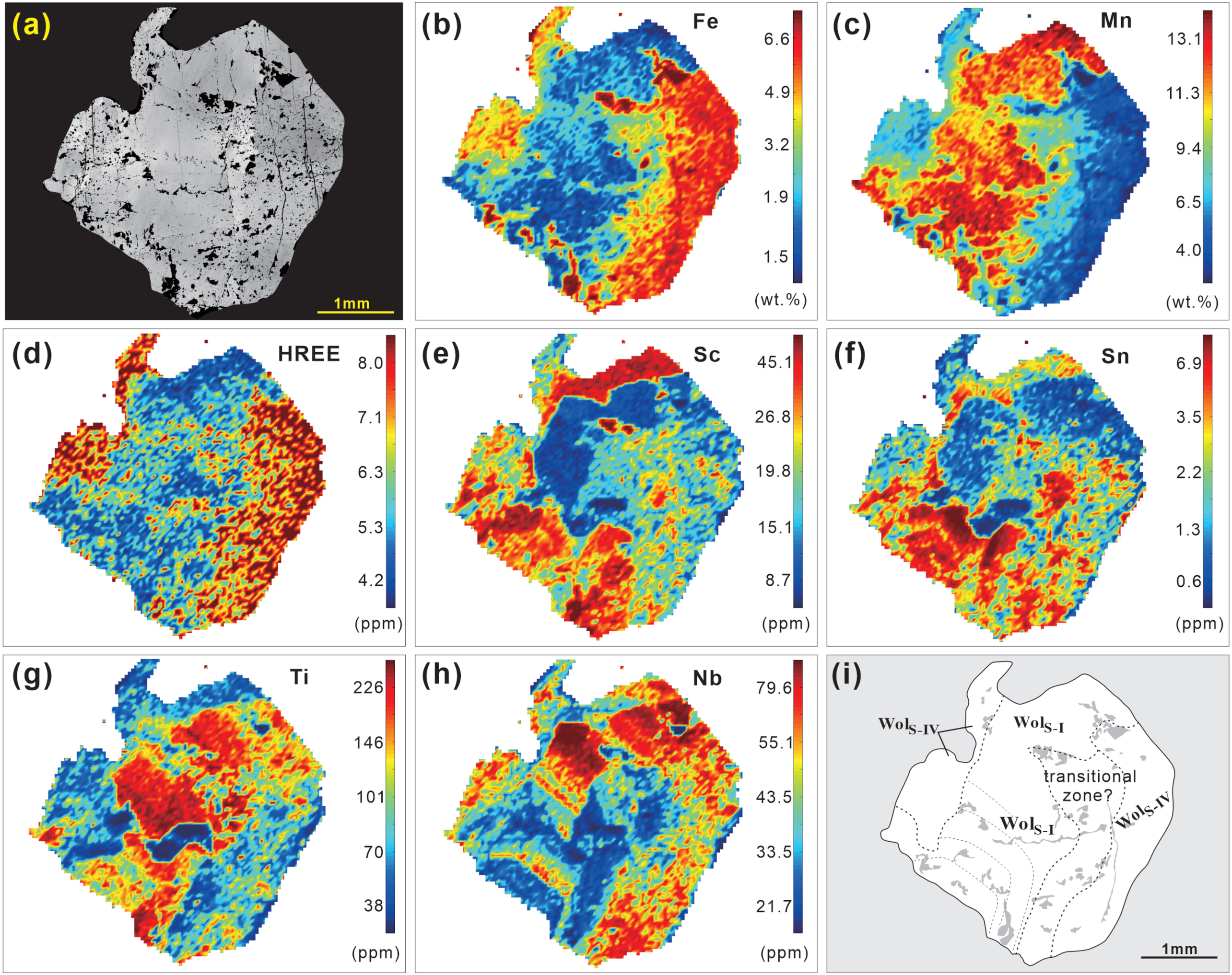
(a)
1mm
(b)
Fe
6.6
4.9
3.2
1.9
1.5
(wt.%)
(c)
Mn
13.1
11.3
9.4
6.5
4.0
(wt.%)
(d)
HREE
8.0
7.1
6.3
5.3
4.2
(ppm)
(e)
Sc
45.1
26.8
19.8
15.1
8.7
(ppm)
(f)
Sn
6.9
3.5
2.2
1.3
0.6
(ppm)
(g)
Ti
226
146
101
70
38
(ppm)
(h)
Nb
79.6
55.1
43.5
33.5
21.7
(ppm)
(i)
Wol S-IV
Wol S-I
transitional zone?
Wol S-I
Wol S-IV
1mm

Figure 9

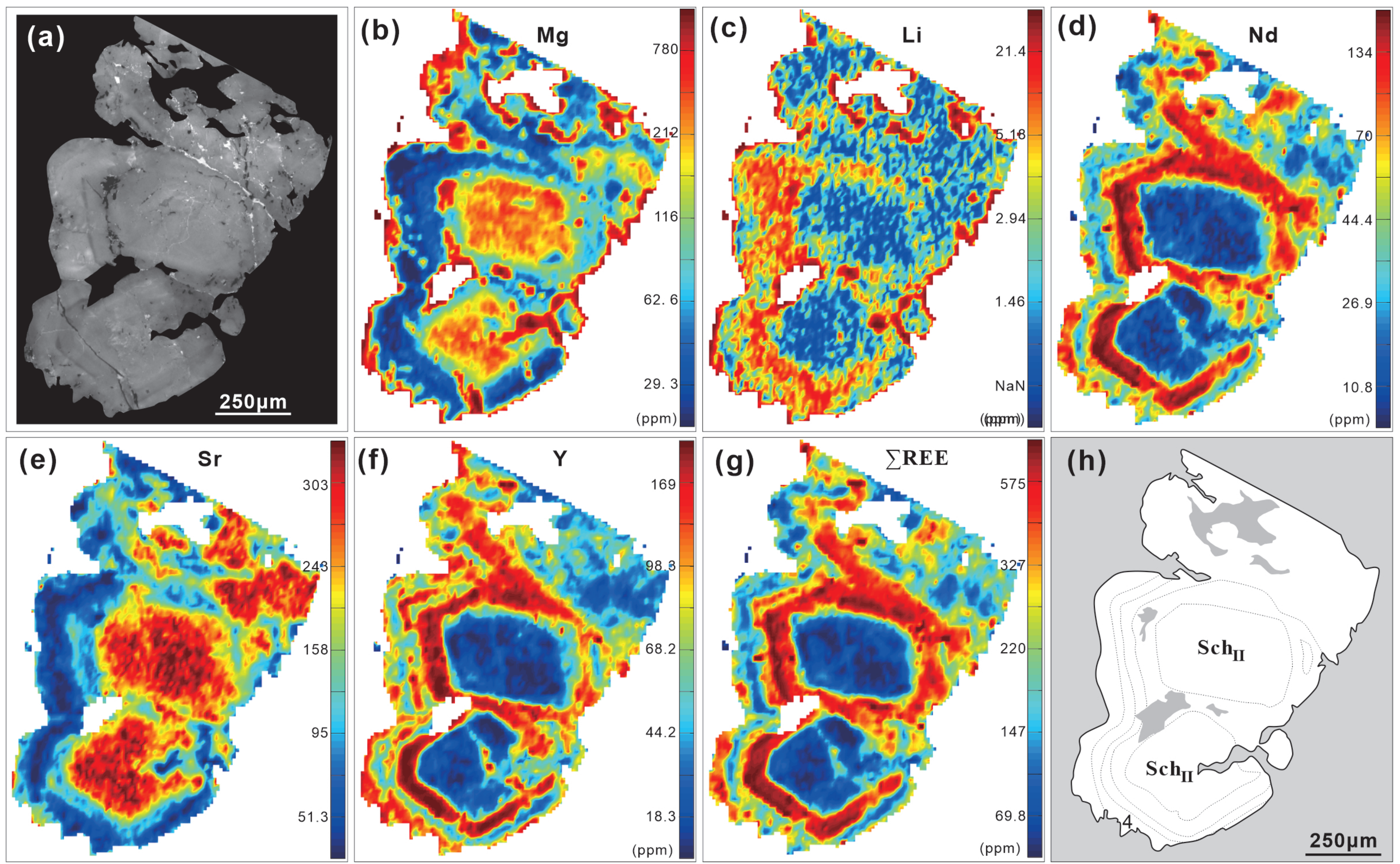
(a)
250μm
(b)
Mg
780
212
116
62. 6
29. 3
(ppm)
(c)
Li
21.4
5.18
2.94
1.46
NaN
(ppm)
(d)
Nd
134
70
44.4
26.9
10.8
(ppm)
(e)
Sr
303
246
158
95
51.3
(f)
Y
169
98.8
68.2
44.2
18.3
(ppm)
(g)
∑REE
575
327
220
147
69.8
(ppm)
(h)
Sch$_{II}$
Sch$_{II}$
4
250μm

Figure 10

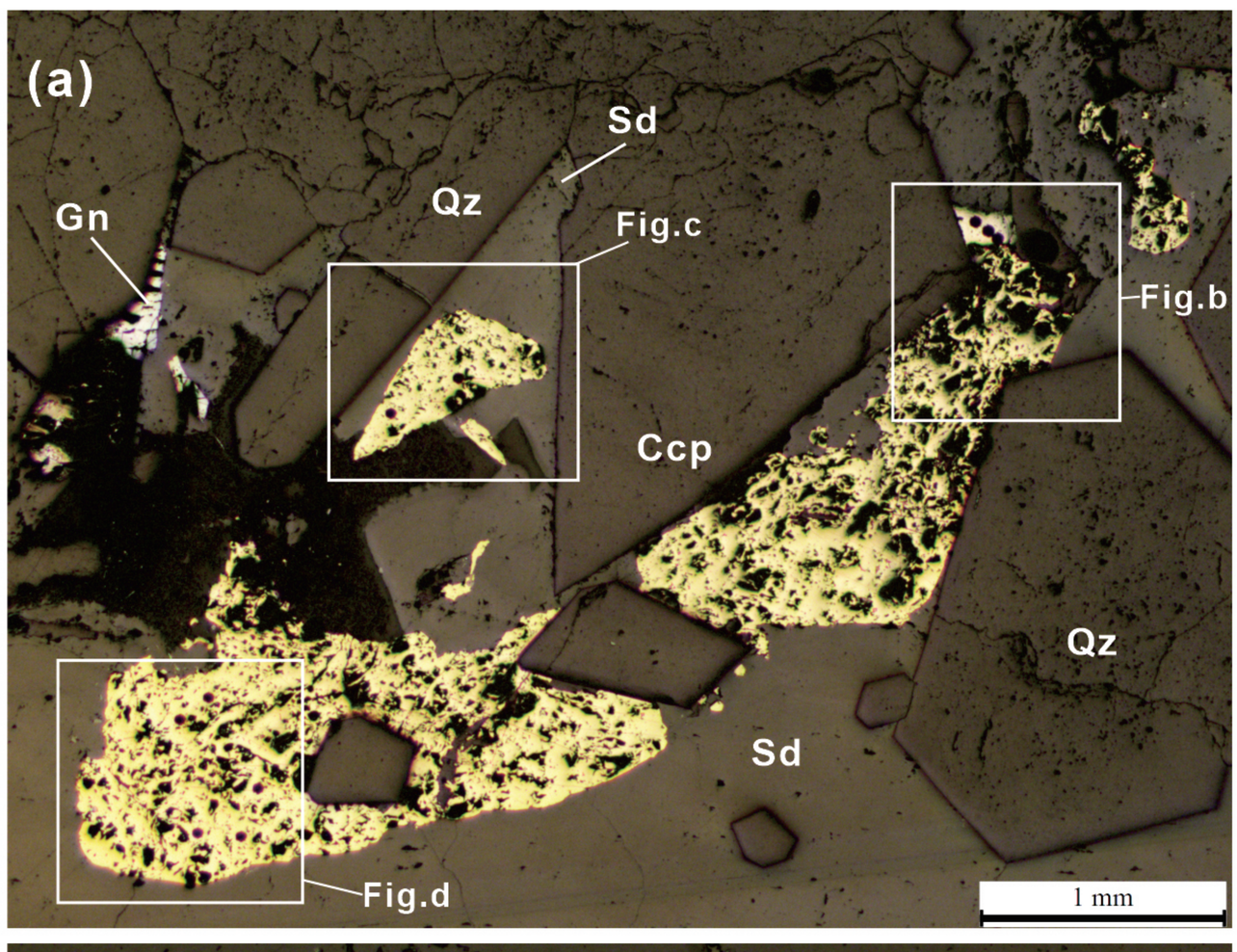
(a)
Sd
Qz
Gn
Fig.c
Fig.b
Ccp
Qz
Sd
Fig.d
1 mm

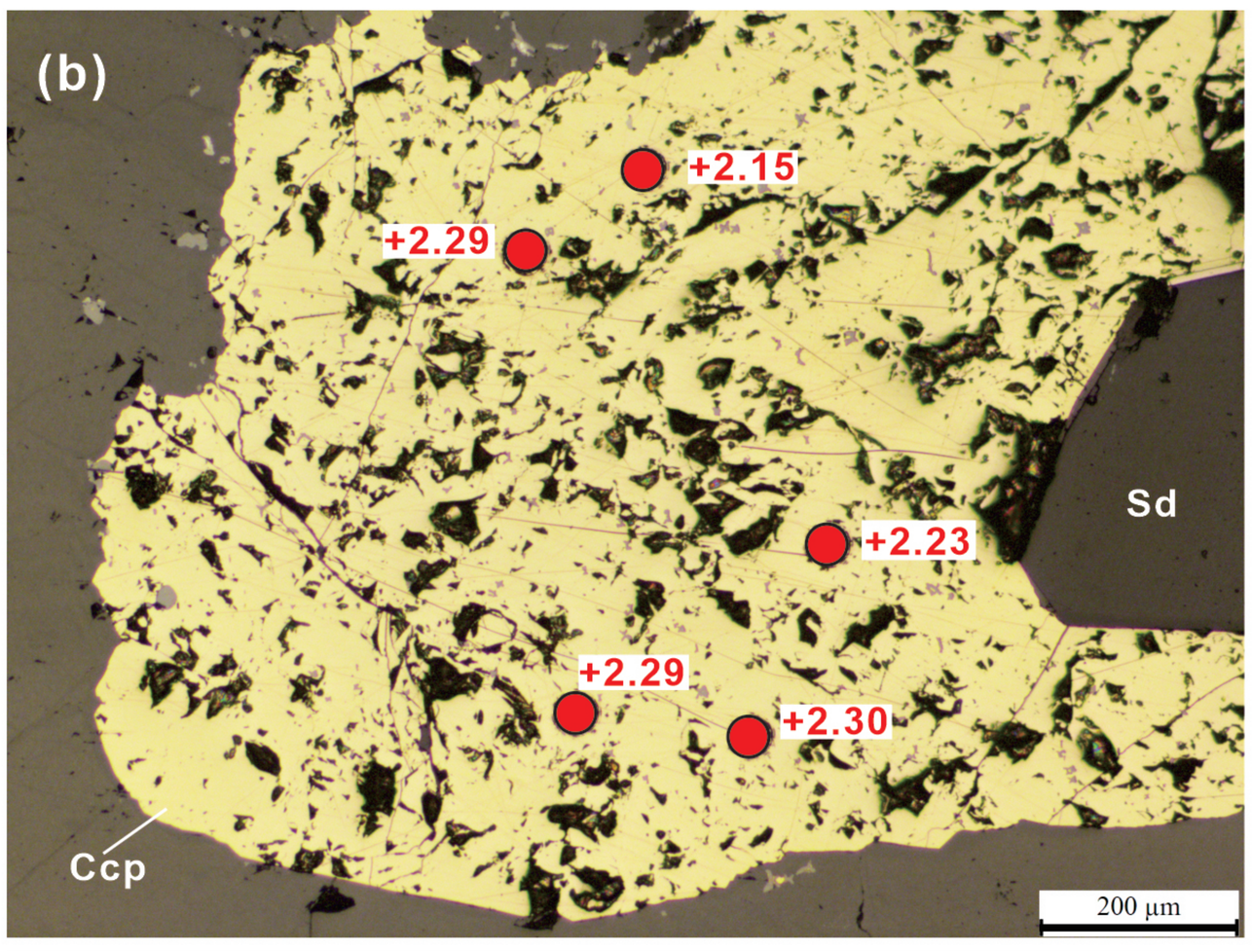
(b)
+2.15
+2.29
+2.23
Sd
+2.29
+2.30
Ccp
200 μm

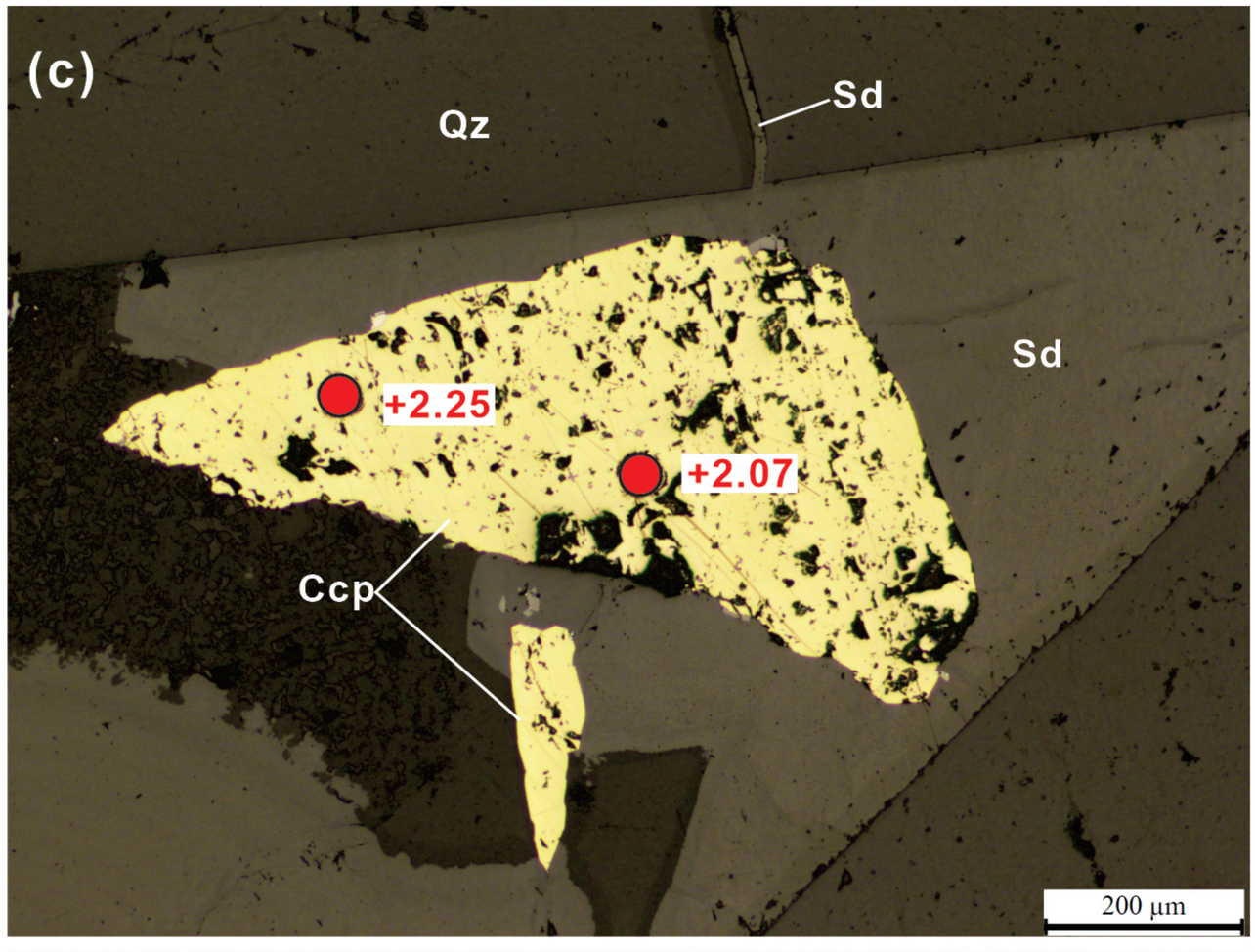
(c)
Qz
Sd
Sd
+2.25
+2.07
Ccp
200 μm

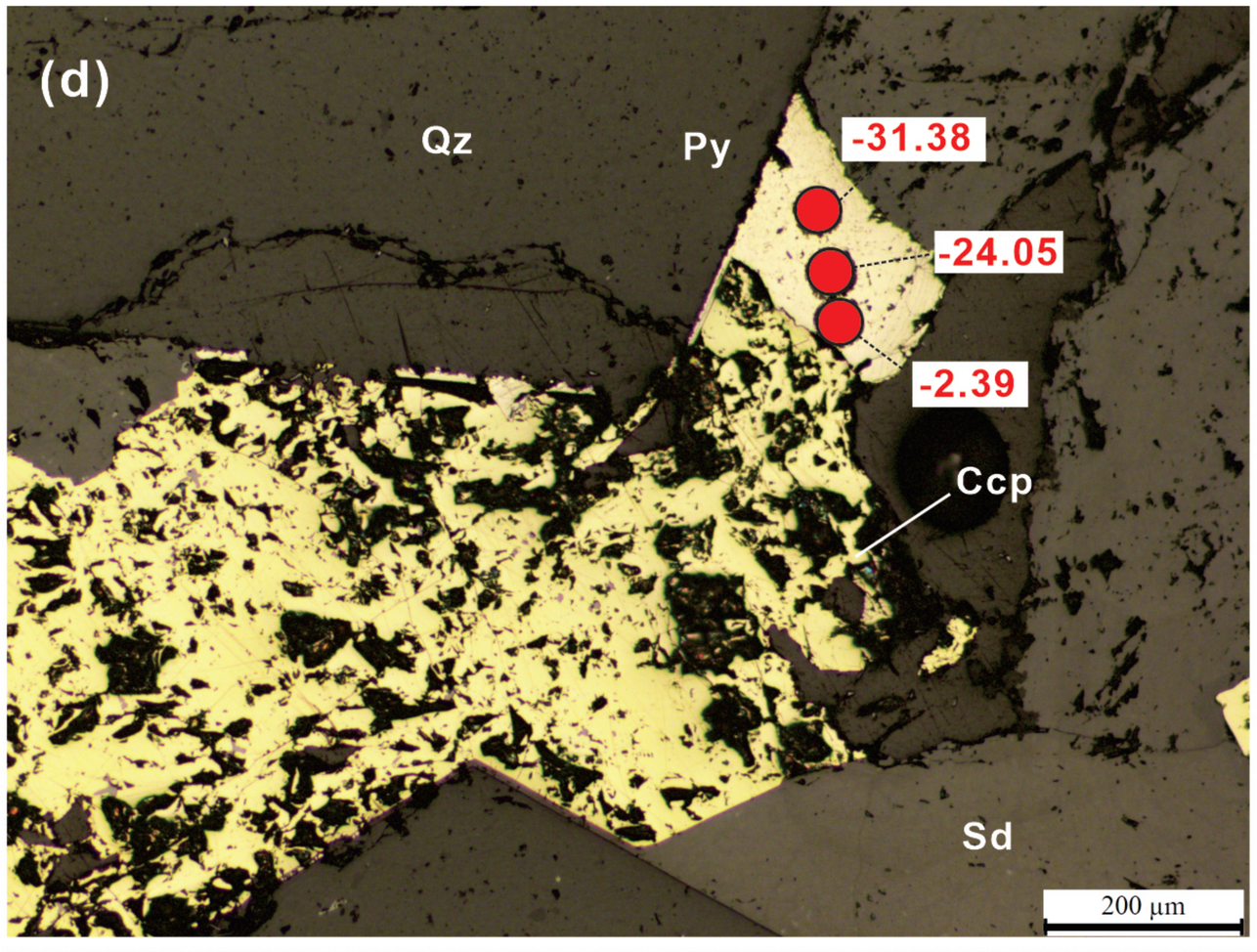
(d)
Qz
Py
-31.38
-24.05
-2.39
Ccp
Sd
200 μm

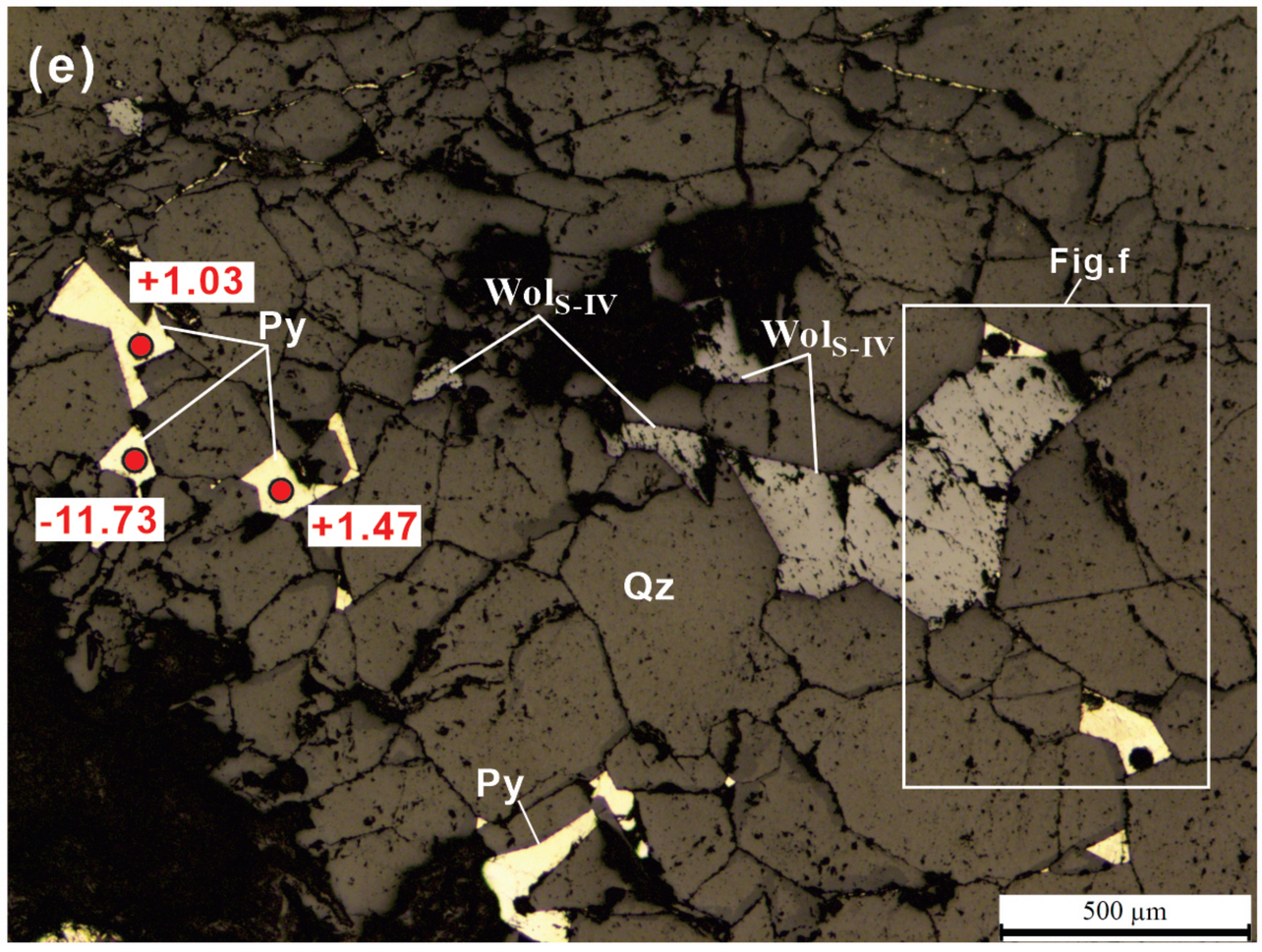
(e)
+1.03
Py
Wol S-IV
Wol S-IV
Fig.f
-11.73
+1.47
Qz
Py
500 μm

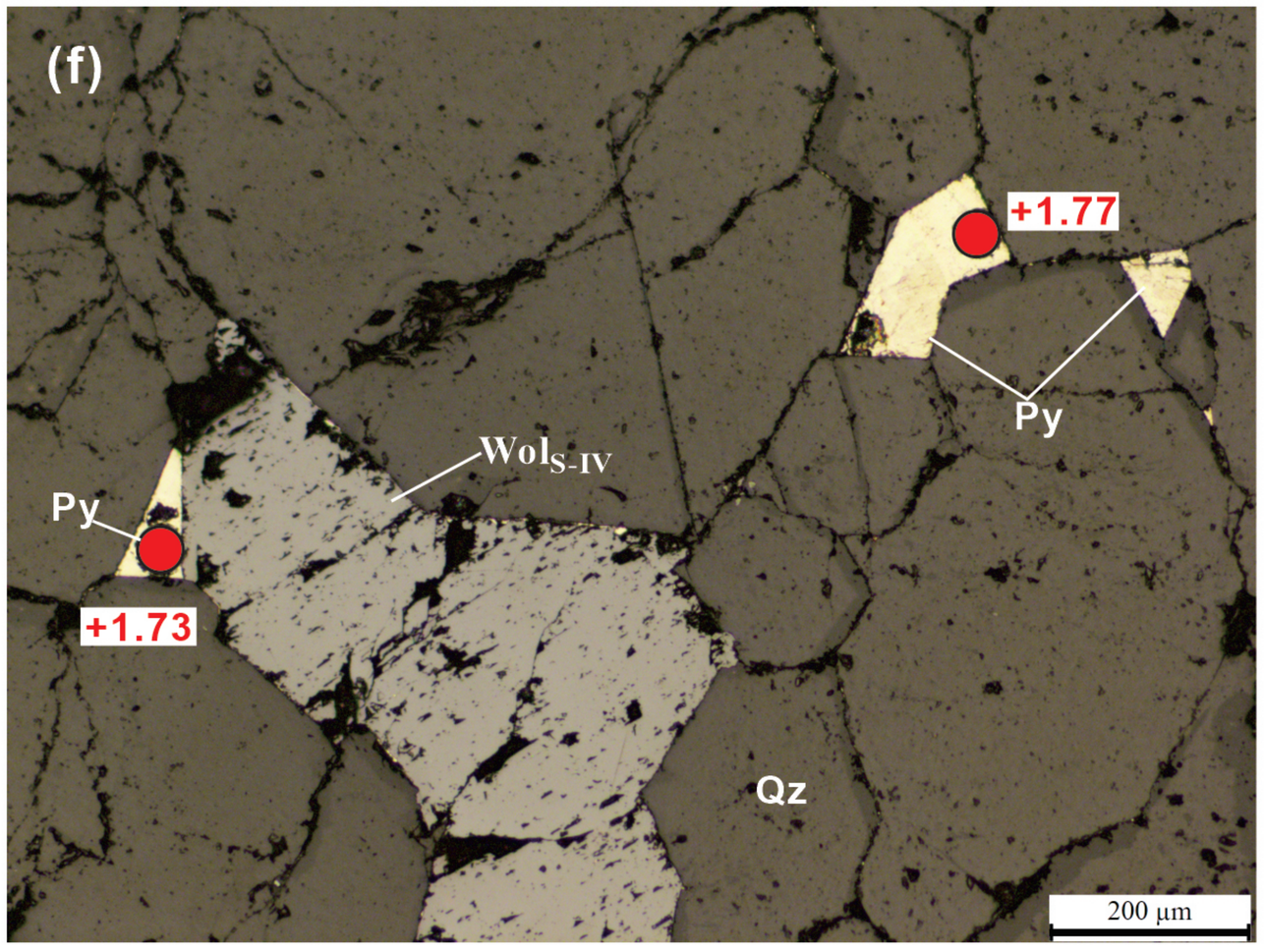
(f)
+1.77
Py
Wol S-IV
Py
+1.73
Qz
200 μm

Figure 11

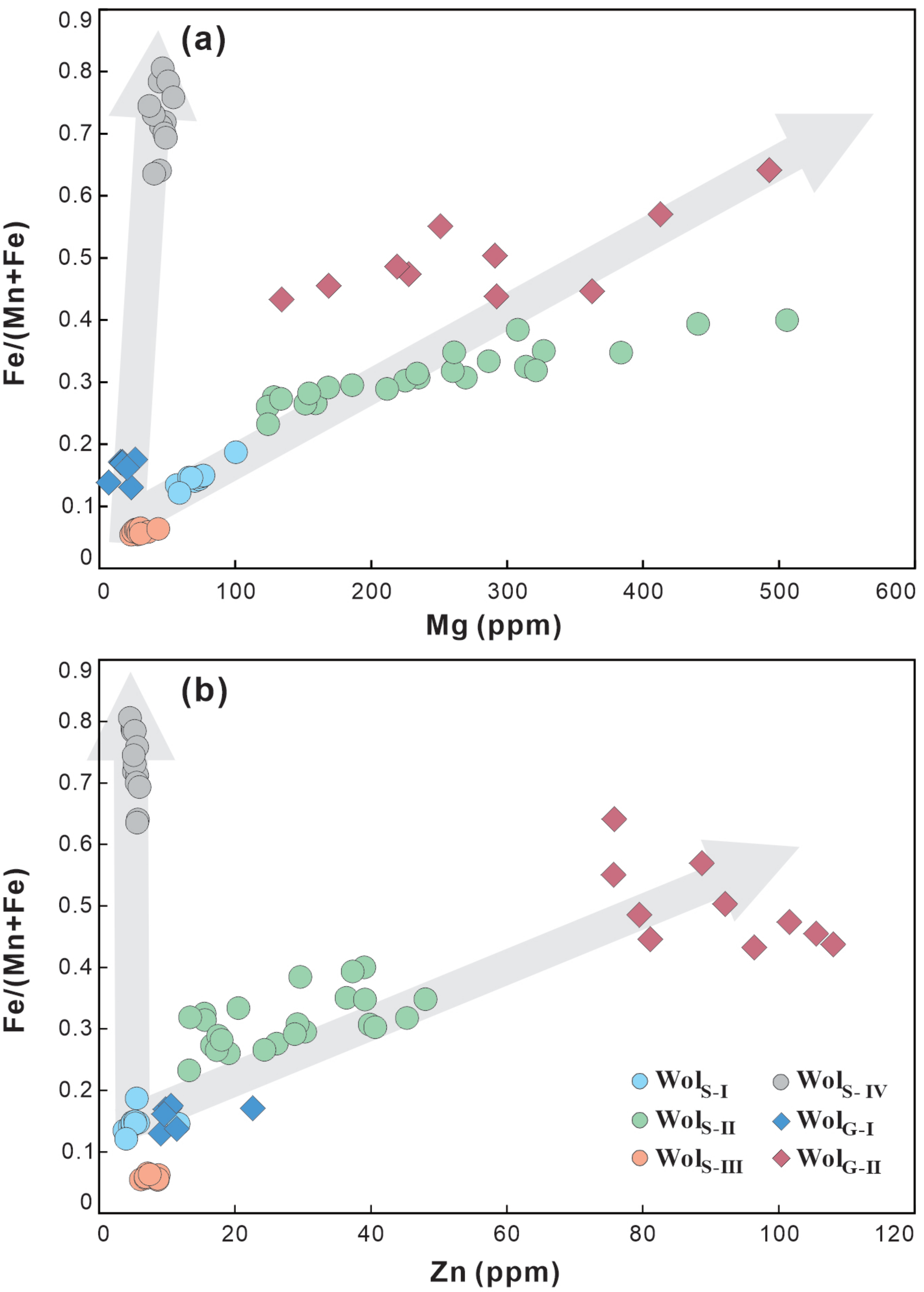
(a)
Fe/(Mn+Fe)
0.9
0.8
0.7
0.6
0.5
0.4
0.3
0.2
0.1
0
0
100
200
300
400
500
600
Mg (ppm)
(b)
Fe/(Mn+Fe)
0.9
0.8
0.7
0.6
0.5
0.4
0.3
0.2
0.1
0
0
20
40
60
80
100
120
Zn (ppm)
Wol S-I
Wol S- IV
Wol S-II
Wol G-I
Wol S-III
Wol G-II

Figure 12

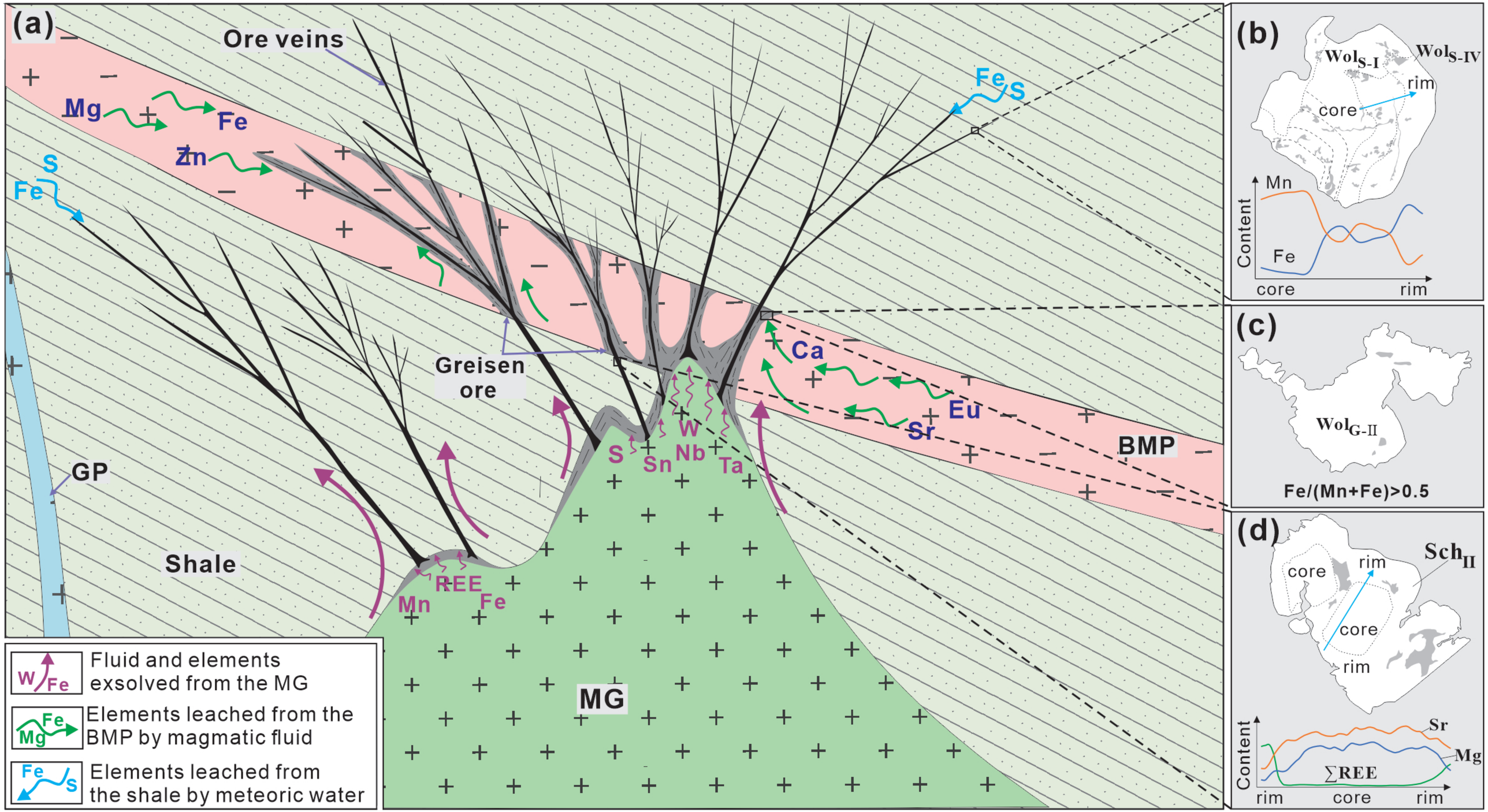
(a)
Ore veins
Mg
Fe
Zn
S
Fe
Fe
S
Greisen ore
Ca
Eu
Sr
BMP
GP
S
Sn
W
Nb
Ta
Shale
REE
Mn
Fe
MG
Fluid and elements exsolved from the MG
Elements leached from the BMP by magmatic fluid
Elements leached from the shale by meteoric water
(b)
Wol S-I
Wol S-IV
rim
core
Mn
Content
Fe
core
rim
(c)
Wol G-II
Fe/(Mn+Fe)>0.5
(d)
Sch II
core
rim
core
rim
Sr
Mg
Content
∑REE
rim
core
rim

Figure 13